CHALMERS
UNIVERSITY OF TECHNOLOGY

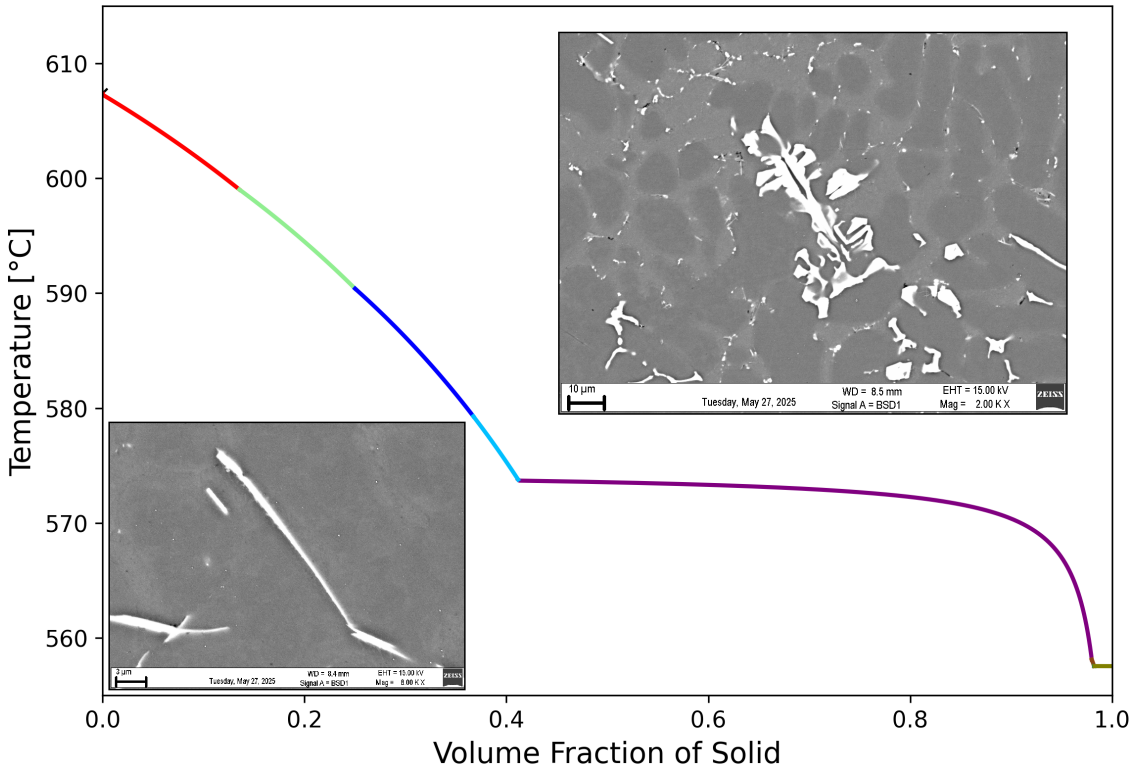

Optimizing the effect of tramp elements on intermetallic phases in HPDC Al alloys – A thermodynamic approach

Master's Thesis in Materials Science and Technology

Nicklas Kaas Ishøy

Department of Industrial and Materials Science
CHALMERS UNIVERSITY OF TECHNOLOGY
Gothenburg, Sweden 2025
www.chalmers.se

Master's thesis 2025

Optimizing the effect of tramp elements on intermetallic phases in HPDC Al alloys – A thermodynamic approach

Nicklas Kaas Ishøy

CHALMERS
UNIVERSITY OF TECHNOLOGY

Department of Industrial and Materials Science
Industrial engineering and management
Chalmers University of Technology
Gothenburg, Sweden 2025

Optimizing the effect of tramp elements on intermetallic phases in HPDC Al alloys – A thermodynamic approach
Nicklas Kaas Ishøy

Supervisor: Deepjyoti Mukherjee, Industrial and Materials Science
Examiner: Fang Liu, Industrial and Materials Science

Master's Thesis 2025
Industrial and Materials Science
Materials and manufacture
Chalmers University of Technology
SE-412 96 Gothenburg
Telephone +46 31 772 1000

Cover: Scheil solidification curve incorporating back-diffusion, shown alongside SEM micrographs illustrating the morphology of the α- and β- phases.

Typeset in LaTeX
Printed by Chalmers Reproservice
Gothenburg, Sweden 2025

Optimizing the effect of tramp elements on Intermetallic phases in HPDC Al alloys – A Thermodynamic approach

Nicklas Kaas Ishøy
Department of Industrial and Materials Science
Chalmers University of Technology

Abstract

The growing interest in increasing the recycled content of aluminium for high-pressure die casting (HPDC) is driven by a demand for greater sustainability, as recycled content offers a ∼nearly 95% reduction in energy compared to primary aluminium. However, elevated levels of elemental contamination from recycled content, mainly tramp elements such as iron (Fe) and manganese (Mn), pose significant challenges. This thesis focuses on the thermodynamic analysis of the Al-Si-Fe-Mn system with additions of magnesium (Mg) by using Thermo-Calc through CALPHAD-based Scheil simulations at a high rate of 100 K/s, in conjunction with validation using complementary microstructure analysis.

The simulations, comprising over 300 compositions, demonstrated a strong linear correlation between increasing Fe content and the fraction of the β-Al_5FeSi phase. In contrast, increasing Mn content suppresses β phase formation by promoting the more benign α-$Al_{15}(MnFe)_3Si_2$ phase. Si notably altered the solidification range and eutectic transitions within the system. Higher Mg levels led to phase competition between π-AlFeMgSi and β phases. The potential evaporation of Mg was also found to shift phase equilibria, increasing the fraction of β phase, emphasising the need for accuracy control of alloy compositions.

Microstructure analysis, employing SEM and EDS on the cast alloys, shows that Fe influences β-intermetallics, as it is composed of Fe instead of Mn. The analysis also reveals compositional variations that influence kinetic effects, such as the formation of the δ-AlFeSi phase and localised solute depletion zones around α-phase particles. These findings clarify the effects of Fe, Mn, Si, and Mg on intermetallic phase formation and emphasise the importance of integrating kinetic effects to contribute to a more comprehensive understanding of optimising recycled aluminium alloys.

Keywords: recycled aluminium, Scheil simulation, HPDC, Thermo-Calc, intermetallic phases, CALPHAD

Acknowledgements

This project was carried out in collaboration between Chalmers and its industrial partners, who kindly provided the samples used in the experimental analysis. Thermodynamic simulations were performed using licenses provided by Thermo-Calc Software AB. Microstructure characterisation was carried out using the facilities at the Department of Industrial and Materials Science, Chalmers University of Technology. I am sincerely grateful to the Engineers of Sweden's Environmental Fund for awarding me the scholarship that supported this work.

I want to express my sincere gratitude to everyone who has supported and contributed to this project. My sincere thanks go to my supervisor, Deepjyoti Mukherjee, for his invaluable guidance, encouragement, and enthusiasm throughout this work.

A special thanks to Sarvesh Saikumar for his work in designing and developing the sample holder and to Xialong Li for his assistance in operating the arc melter used for casting the samples. I am also deeply grateful to my examiner, Fang Liu, whose introduction to the topic regarding recycled aluminium opened the door for me to further contribute to this research area with my thesis.

On a personal note, I extend heartfelt thanks to my wife and daughter for their unwavering support, patience, and motivation during this journey. Finally, I would like to acknowledge my classmates, Guokang Li and Jihui Yang, for their companionship and collaboration throughout the past two years.

Nicklas Kaas Ishøy, Gothenburg, June 2025

List of Acronyms

Below is the list of acronyms that have been used throughout this thesis listed in alphabetical order:

BSE	Back-Scattered Electrons
CALPHAD	Computer Coupling of Phase Diagrams and Thermochemistry
EBSD	Electron Backscatter Diffraction
EDS	Energy-Dispersive X-ray Spectroscopy
FIMC	Fe-containing Intermetallic Compounds
HPDC	High Pressure Die Casting
IMC	Intermetallic Compounds
OES	Optical Emission Spectroscopy
RC	Recycled Content
SDAS	Secondary Dendrite Arm Spacing
SEM	Scanning Electron Microscopy
SE	Secondary Electrons
SF	Sludge Factor
SOM	Stereo Optical Microscopy

Contents

List of Figures

List of Tables

1
Introduction

1.1 Background

Aluminium, the metal with the second-highest global demand, is expected to have a production increase from 110 million metric tons in 2022 [1] to 180 million tons in 2050 [2]. This increase is primarily driven by the growing demand in various sectors involved in the green transition, primarily through efforts to achieve more sustainable manufacturing practices by incorporating a higher proportion of recycled aluminium [3]. This thesis project focuses on the transportation sector, where Al alloy is used in developing the core structure of electric vehicles. Notably, reducing a vehicle's weight by just 10% can lower energy consumption by 3.2-6.8%. Aluminium alloys, with only one-third the density of steel, offer significant weight reduction potential that can substantially decrease a vehicle's carbon footprint over its entire life cycle [4].

Although aluminium is essential for the green transition, its production from bauxite ore poses significant sustainability challenges. The process is highly energy-intensive and generates significant greenhouse gas emissions, pollutants and solid waste. In total, aluminium production contributes approximately 1.1 gigatons of greenhouse gases per year, accounting for about 3% of annual global greenhouse gas emissions. With more than half of the greenhouse gas emissions linked to electricity, it is essential to note that primary aluminium production is highly energy-intensive, consuming approximately 960,000 GWh, corresponding to $\sim$ around 1% of global energy consumption in 2023 [5].

On the other hand, aluminium is almost infinitely recyclable, with 75% of all aluminium ever produced still in circulation today. Recycling aluminium is highly energy efficient, requiring only 2.8 kWh/kg compared to 45 kWh/kg for primary production, resulting in a $\sim$ 95% reduction in energy consumption and a similar ($\sim$ 95%) reduction in pollutants [3].

Nonetheless, using secondary aluminium alloys poses serious challenges. Recycled aluminium alloys often have a broad composition window. In contrast to steel, aluminium alloys have a low solubility for many elements, making them sensitive to impurities. The conventional method of handling this is by diluting the concentration by adding a significant amount of primary aluminium. However, this approach becomes impractical as the portion of aluminium increases to support a more circular

production process. While some unwanted elements can be removed, the extraction of certain impurities, particularly Fe, is often limited by economic constraints [6]. This impurity sensitivity presents a significant challenge for manufacturers aiming to increase recycled content without compromising product quality. This is especially important for Al alloys, as they are widely used in High-Pressure Die Casting (HPDC), a manufacturing technique by the automotive industry, which faces severe challenges due to the variable microstructure and defects that are enhanced by the use of recycled aluminium [3].

1.2 Problem statement

As the demand for recycled aluminium increases due to greater sustainability, the integration of increased content of tramp elements, such as Fe and Mn, is sought for HPDC alloys. Impurities promote the formation of brittle intermetallic phases and negatively impact the predictability of the microstructure and their performance. Conventional thinking through strategies such as using primary alloys has to be challenged to create a circular production chain. Thus, a deeper understanding of how Fe, Mn, Si, and Mg and their interactions during solidification is needed to control certain phases influenced by recycled content and to achieve better quality.

1.3 Aim and research question

The aim of this is to investigate and control the effect of tramp elements (due to high recycled content) on the formation of certain intermetallic phases in the Al-Si-Fe-Mn system from a thermodynamic point of view.

This research question was defined as follows: How can compositional control and thermodynamic modelling be used to predict and optimise intermetallic phase formation in recycled Al–Si–Fe–Mn alloys under high cooling rate conditions?

1.4 Delimitations

The primary focus of this work is to understand the microstructural evolution of Al-Si-Fe-Mn alloys, with minor additions of Mg, during solidification. The emphasis of this thesis lies on the formation, morphology and composition of Fe- and Mn-rich intermetallic phases, specifically the Al_5FeSi and α-$Al_{15}(Fe,Mn)_3Si_2$ phases. This is achieved by employing a thermodynamic approach, which involves a combination of computational thermodynamics, specifically CALPHAD-based Scheil-Gulliver simulations, and validation through complementary microstructural characterisation analysis techniques, including SEM imaging and secondary dendrite arm spacing measurements.

To outline a clear definition and research scope, the following delimitations are established:

- **Alloy Composition:** This study is based on the Al–Si-Fe-Mn alloys with varying Si, Fe and Mn content with some Mg additions. Other alloying or trace elements such as Cu, Cr, and Ni are excluded from the analysis.

- **Focus on tramp elements:** Fe and Mn are considered the primary tramp elements influencing the formation of α- and β-intermetallic phases. Mg is included to assess its role in modifying the solidification path, its interplay with Fe and Mn and its interaction with the β- and π-phases.

- **Influence of Si and Mg:** The study investigates how increasing Si and decreasing Mg content affect intermetallic formation and solidification behaviour. Special attention is given to potential Mg and Al losses due to evaporation and how it alters the solidification path.

- **Scheil Simulation Model:** Thermodynamic modeling is performed exclusively using Scheil–Gulliver method with back-diffusion simulations in the Thermo-Calc TCAL9 and MOBAL8 databases. Advanced kinetic models, such as DICTRA, are considered beyond the scope of this thesis.

- **Experimental Characterisation:** Experimental work is limited to microstructural analysis using SEM and SDAS measurement. No mechanical property testing or advanced crystallography, such as EBSD, is conducted.

- **Casting method:** The investigation is based on solidification conditions at high cooling rates representative of high-pressure die casting, which is done through arc-melted samples.

2

Theory

The current trend of thinking regarding cast aluminium metallurgy can be summarised in the following general points. Pores are an intrinsic part of aluminium castings; they can only be minimised and controlled to a certain extent. The single most important microstructure parameter is the secondary dendritic arms spacing (SDAS), as it affects almost all mechanical properties: yield and tensile strength, elongation to failure, and fatigue resistance. It is essential for controlling ductility along with other mechanical properties.

However, intermetallic phases such as β-Al_5SiFe, which have a platelet-like morphology, are weak and brittle and can cause premature fracture in castings, reducing mechanical properties such as ductility. Additionally, in Al-Si alloys, the size of the Si-diamond phase in the eutectic region needs to be controlled because these particles fracture and deform in the early stages of plastic deformation, serving as the local cause of crack formation that leads to premature failure [7, 8].

In recent years, significant improvements have been made to casting techniques, resulting in a reduction in the number of casting defects in Al alloys. Consequently, other parameters, such as microstructure, secondary dendritic arm spacing (SDAS), grain size, the size and morphology of eutectic Si particles, and the shape and distribution of intermetallic compounds, need to be considered more extensively to accurately predict the mechanical behaviour and properties of cast Al alloys [8].

2.1 Aluminium metallurgy

Generally, four tons of bauxite generates two tons of alumina, which in turn yields one ton of aluminium. The mining process itself, for the same amount, generates roughly 10 tonnes of waste rock and 3 tonnes of toxic "red mud" [9]. According to the U.S. Geological Survey [10], global bauxite reserves are estimated to range from 55 to 75 billion tonnes, with the largest shares located in Africa (32%), Oceania (23%), South America and the Caribbean (21%), and Asia (18%), while the remaining (6%) is distributed elsewhere.

After the bauxite ore has been mined, it is then reduced to alumina (aluminium oxide) by using the Bayer process, where the bauxite is processed using sodium hydroxide under pressure and varying temperatures. This process removes the vast majority of impurities from bauxite, producing a by-product known as red mud.

The remaining material is then processed, reducing it to aluminium using the Hall-Héroult process, a very energy-demanding process [9].

In a comprehensive article by Raabe et al. [3] on the topic of the integration of higher circularity for aluminium. The authors argue that traditional alloys were not designed with the metallurgical knowledge we have today, nor do they meet the demand for higher integration of recycled content. Sustainable alloys containing high recycled content should be developed with clearly defined maximum scrap tolerances, meaning they should show high tolerance to tramp elements and minor composition variations. This is particularly important for aluminium, given its inherently low solubility of many elements. The authors also stress the need to reduce dependency on rare and costly elements; when such elements are used, they should be recoverable through efficient methods to minimise waste and prevent landfill disposals.

The article outlines several metallurgical research topics for this transition. One key area is "the influence of scrap-related contaminant elements on the thermodynamics and kinetics of precipitation reactions". Raabe further highlights the importance of precise microstructural control for specific applications and for promoting alloy simplification by using fewer alloying elements for the ease of future recycling of aluminium scrap. This is especially relevant for the current and future use of HPDC, of which over 50% of all aluminium alloys are used using the manufacturing process, where variable microstructure is an intrinsic part of the casting process.

2.1.1 High-pressure die casting

HPDC is known for producing products with excellent surface finishes and precise geometric accuracy. The molten metal is injected into a die cavity at high velocities using a shot sleeve and piston system. The process uses rapid filling and solidification speed; a schematic of HPDC can be seen in Figure 2.1. These facts make HPDC suitable for industries that employ mass production. However, the rapid filling of the die introduces challenges such as oxide bifilms, entrained air, and variable microstructure, which contribute to porosity and internal defects.

To combat these downsides, vacuum-assisted HPDC is often used in Al-Si castings by expelling air from the die cavity before and during the injection of the mould, which reduces gas porosity and minimises air entrapment, leading to improved mechanical properties in HPDC. Molten aluminium alloys can lead to evaporation of volatile elements, especially Mg, due to its relatively low boiling point at $\sim$1090 °C compared to aluminium at $\sim$2470 °C. Evaporation can be mitigated by melting and casting in an inert gas, such as argon, which significantly reduces the rate of evaporation [11].

Furthermore, there are two main factors determining the rate of vaporisation: high temperatures or reduced pressure. Vacuum systems in die casting can achieve pressures as low as 50 mbar [11, 12]. Research has shown that under melting conditions

of 60 Pa and ∼ approximately 1484 °C, aluminium losses can reach 11.5%, which demonstrates the impact of low pressure and high temperature on Al evaporation [13].

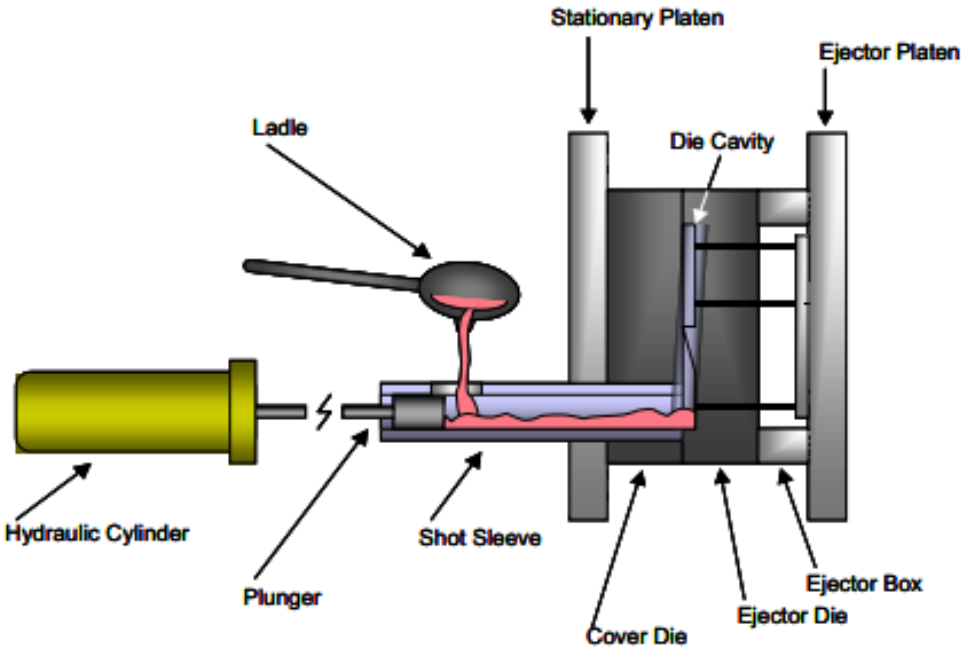

Figure 2.1: Schematic of a cold chamber die-casting machine. The diagram illustrates the key components, including the plunger, shot sleeve, and die cavity. Adapted from [14] licensed under CC BY-SA 4.0. Licence: https://creativecommons.org/licenses/by-sa/4.0/

2.2 Effect of alloying elements

Most metals will alloy with aluminium; however, compared to other metals, few elements have sufficient solid solubility to act as major alloying elements (>10 wt.%). Of the common elements used, only zink and Mg have a high level of solubility. Most other elements have their maximum solubility well below 1 wt.%, usually observed at eutectic temperatures. In Table 2.1, these values are summarised for the examined elements in this thesis.

Table 2.1: Maximum solid solubility of examined elements in aluminium [15].

Element	**Temperature (°C)**	**Maximum solid solubility**	
		(wt.%)	**(at%)**
Silicon (Si)	577	1.65	1.59
Iron (Fe)	655	0.05	0.025
Manganese (Mn)	658	1.82	0.90
Magnesium (Mg)	450	17.4	18.5

Si, Silicon: It is the primary element added to die-casting alloys, with the primary purpose of significantly improving castability due to its low melting range and enhancing fluidity. Allowing for the filling of the mould in thin sections and complex shapes to reduce the amount of defects. The improvement in fluidity is attributed to the high latent heat of fusion of Si, which is released during the feeding process. Another castability parameter which is improved by the addition of Si is hot-tearing, which occurs due to the thermal contraction mismatch during solidification. Unlike most elements, Si expands upon solidification, partially compensating for the shrinkage of the aluminium matrix. The expansion enhances the alloy's fluidity during the final stages of solidification, thereby reducing the risk of shrinkage porosity [16].

Generally, a balance between fluidity and mechanical properties is desired. Higher Si yields higher fluidity up until the hyper-eutectic region at 14-16 wt.% (in contrast to other alloys where the maximum fluidity occurs at the eutectic region), whereas lower Si in the hypo-eutectoid area of ∼5-9 % is used when higher ductility or heat treatment with Mg is preferred [17].

Fe, Iron: The main benefit of Fe is that it improves castability. It increases hot-tear resistance and reduces die soldering, a casting inconvenience, where the molten aluminium sticks to the steel die. Therefore, Fe is typically kept as low as possible for the casting needs. Fe is often referred to as an impurity, commonly found in aluminium alloys and is almost always present in cast Al-Si alloys in the range of 0.1-0.8 wt.% coming from scrap/recycled metals and from contact with steel tools. Fe has a high solubility in the liquid state, but only 0.05 wt.% in the solid state, as summarised in Table 2.1. This means Fe, over the maximum solid solubility, will solidify as intermetallic compounds in combination with aluminium. A high degree of Fe decreases the ductility from the formation of the intermetallic β-Al_5SiFe phase [18].

The presence of Si promotes the formation of Al-Fe-Si intermetallic compounds, the two most common FIMC are the β-phase, Al_5SiFe, and the α-phase $Al_{15}(MnFe)_3Si_2$, which will be discussed more thoroughly in section 2.2.1. At levels up to ∼0.2 wt.%, the intermetallics appear small; however, approaching higher levels at ∼1.0 wt.% will increase their volume fraction considerably. This rise in intermetallic content makes them more brittle and results in darker contrast under optical microscopy during microstructure analysis. The morphology and type of FIMC are influenced by other alloying elements, particularly Mn. In the absence of Mn, Fe predominantly forms brittle β-phase platelets. However, at higher Mn levels—or lower Fe/Mn ratios—the formation shifts toward the more favourable α-phase, which exhibits a more compact morphology and improved mechanical compatibility [16].

Mn, Manganese: It is a minor alloying element used in most cast aluminium alloys. Recycled aluminium often contains high Mn, carried over as a tramp element. In Al-Si cast alloys, Mn usually controls the Fe-rich intermetallic phases. It improves ductility of alloys containing Fe and Si modification of β-Al_5FeSi intermetallic inclusions from platelet/acicular to the cubic form of α-$Al_{15}(MnFe)_3Si_2$. The latter should be the primary intermetallic phase, as it offers better mechanical

properties than Al_5FeSi, as Mn can substitute Fe. Thus, in Al-Si cast alloys, Mn is generally considered a Fe mitigator as it suppresses the formation of β phases. A too-high wt.% of Mn can lead to a "sludge factor" where coarse agglomerates of α-$Al_{15}(MnFe)_3Si_2$ form instead of the desired fine particles, leading to degradation of mechanical properties [19].

Additionally, Mn can indirectly influence the grain size and SDAS by altering the solidification sequence and, specifically, promoting the precipitation of FIMC in the inter-dendritic regions. Since these particles do not serve as nucleation sites for the aluminium matrix, their presence subtly affects the dendritic growth pattern, thus indirectly modifying the dendritic growth pattern [16, 11].

Mg, Magnesium: In Al-Si alloys, Mg is typically added as a secondary element; one particular role is to improve the machinability as it makes the alloy more responsive to cutting, which is thought to be due to its effect on chip formation. The primary reason for Mg is that it acts as a basis for enhancing strength and hardness through heat treatment. Without the addition of Mg, the Al-Si alloys will retain their as-cast strength state.

Essentially Mg is added to form Mg_2Si phase particles which can be heat-treated through precipitation hardening. Mg, as a minor alloying element, does not drastically change the as-cast macrostructure's appearance; its real effect is seen after heat treatment when a dense dispersion of fine precipitates is present, aside from a few small Mg_2Si intermetallics [16].

2.2.1 Secondary phases

Fe has very low solubility in aluminium in the solid state (∼0.05 wt.%), which promotes the formation of secondary FIMCs during solidification of aluminium alloys. Over 20 FIMCs have been identified in Al alloys. Among them, the most common in cast aluminium are:

- $\beta - Al_5FeSi$ (platelet morphology)
- $\alpha' - A_8Fe_2Si$ (script-like morphology)
- $\alpha - Al_{15}(Fe, Mn)_3Si_2$ (compact Chinese script)
- $\delta - Al_4FeSi_2$ (smaller platelet morphology, metastable phase)

Each of these phases forms under different compositional and thermal conditions while influencing the mechanical behaviour differently [20]. Table 2.2 summarises the crystal structures of these key Fe-containing intermetallics observed in Al-Si-Fe-Mn alloys; the crystal structures' characteristics influence the morphology and mechanical properties of the cast microstructure.

Table 2.2: Crystal structure information for selected Fe-containing intermetallic phases in the Al-Fe-Si and Al-Fe-Mn-Si systems.

Phase	Composition	Space Group	Lattice Parameters (Å)	Ref.
τ_4 or δ	Al_4FeSi_2	Tetragonal I4/mcm	$a = 6.07$ $c = 15.221$	[21]
τ_5 or α'	Al_8Fe_2Si	Orthorhombic Cmcm	$a = 7.995$ $b = 15.162$ $c = 15.221$	[21]
τ_6 or β	$Al_{4.5}FeSi_2$	Monoclinic A2/a	$a = 6.61$ $b = 8.95$ $c = 20.438$ $\beta = 90.13°$	[21]
α-Al(Fe,Mn)Si	$Al_{15}(Fe,Mn)_3Si_2$	Cubic $Pm\bar{3}$ Cubic $Im\bar{3}$	$a = 12.65$ $a = 12.56$	[21]

β-Al_5FeSi: The β-phase is always a primary phase; it has a three-dimensional form of a platelet, which takes the form of needles when viewed with the use of a two-dimensional optical micrograph. It is most associated with a Fe content higher than 1 wt.%, which roughly coincides with the eutectic point in the Al-Si–Fe phase diagram. However, if there is enough segregation of Fe during solidification, it causes the β-phase to form, even if the Fe content is lower than 1 wt.% [22]. The β-phase has widely been reported to vary within the stoichiometric compositions of $Al_9Fe_2Si_2$, Al_9FeSi, $Al_{13,6}Fe_3Si_{3,05}$, $Al_{13,3}Fe_3Si_{3,3}$, and $Al_{13,6}Fe_3Si_{3,4}$. The β-Al_5SiFe chemical formula has been widely accepted to describe this phase. [22]

The addition of alloys such as Mn and Sr is used to reduce the amount of β-phases and their adverse effects. In a study of the effects of alloying elements on strength and ductility, a quality index score was developed for high-pressure die casting alloys. The study showed that the alloy quality was strongly influenced by the additions of Mn and Cr, which refine the Fe-rich phases, and by Sr, which modifies the eutectic Si morphology. Sr was found to have a greater effect below Fe 0.6 wt% due to its effects causing fragmentation on β-Al_5SiFe phase platelets. In contrast, Cr and Mn have a better corrective effect at Fe higher than 1.5 wt% [22].

The addition of Mn improves the ductility of alloys containing Fe and Si by modification of β-Al_5SiFe intermetallic inclusions from platelet/acicular to cubic form to the $Al_{15}(MnFe)_3Si_2$. [23] The former should be the primary intermetallic phase, as it offers better mechanical properties than Al_5FeSi, as Mn can substitute Fe. Thus, Mn is generally considered a Fe mitigator due to the decrease in the formation of β-phases. A Fe/Mn ratio of 0.5 is commonly used. However, too high a content of Mn can lead to sludge formation, where α particles form before the eutectic structure, resulting in large clusters of α-$Al_{15}(MnFe)_3Si_2$ instead of small particles. Resulting in the degradation of mechanical performance [19]. As a general guideline, an overall

amount of Mn + Fe should not exceed 1-1.5 wt.%, as there is an increased risk of sludge formation [24].

δ-Al_4FeSi_2: For the metastable phase δ-Al_4FeSi_2 to form, it is necessary for the local liquid compositions to be relatively high in both Fe and Si with a Fe: Si ratio of $\sim$1:2 before crystallisation can occur. Two key factors promote δ phase formation: high Si content (minimum 8 wt.%) and rapid solidification (which limits diffusion). High Si content may drive the composition of the remaining liquid toward the δ-phase, which may favor the nucleation of the δ-phase instead of the β or α phases. Rapid solidification rates allow metastable phases to form, such as δ instead of an equilibrium phase, in this case, the β-phase.[24]

The effect of Mn on the δ-phase formation remains unknown, even though the solidification path in Al-Si alloys has been widely studied over a wide range of Si, Fe, and Mn contents, as well as different cooling rates. Studies suggest that kinetics is the primary reason for the formation of the δ-phase. Their plate-shaped morphology, similar to that of the β-phase, makes it difficult to differentiate between the two phases reliably and, thus, may easily be overlooked. Both β- and δ- appear with the same Fe content and comparable (Al + Si) molar fractions; however, the β-phase typically contains less Si and more Al than the δ-phase. The composition similarity, combined with their narrow platelet morphology and recurrent residence in the Al-Si eutectic region, makes them difficult to distinguish using techniques such as EDS, which relies on local chemical measurement. Reliable identification of these phases requires techniques which distinguish intermetallics based on their crystallographic structure rather than solely on chemical composition, such as EBSD [25].

α-$Al_{15}(MnFe)_3Si_2$: Mn is commonly added to suppress the formation of the detrimental τ_5: α-Al_8Fe_2Si and τ_6: β-$Al_9Fe_2Si_2$ phases, via formation of the more sought after α-AlFeSi phase, defined as: $Al_{15}Si_2M_4$, where M can be substituted to be Cr, Fe, Mn, Mo [26]. With a lower Fe/Mn ratio, these dispersoids have a simple cubic (SC) crystal structure, while with a higher Fe/Mn ratio, they have a BCC structure; the transition depends on the Fe/Mn ratio [21].

Research has shown that, except for primary α-$Al_{15}(MnFe)_3Si_2$, which is characterised by its compact morphology and relatively fine size. In contrast, the α-phase that forms within the eutectic region typically exhibits a Chinese script morphology. This phase can grow to a massive scale in three dimensions—often several hundred micrometres or more, which is detrimental to the mechanical properties of the alloy. Morphology control and refinement of Fe-intermetallics are, therefore, some of the key aspects when it comes to improving the mechanical properties of Al alloys [20].

Both of the α phases, α-$Al_{15}(MnFe)_3Si_2$ and Al_8Fe_2Si, form with a Chinese script morphology; however, $Al_{15}(MnFe)_3Si_2$ is found to be more compact. This is in contrast to the platelet morphology of Al_5SiFe. In Figure 2.2, Al_5SiFe and α-$Al_{15}(MnFe)_3Si_2$ show their distinct morphologic characteristics as seen in SEM.

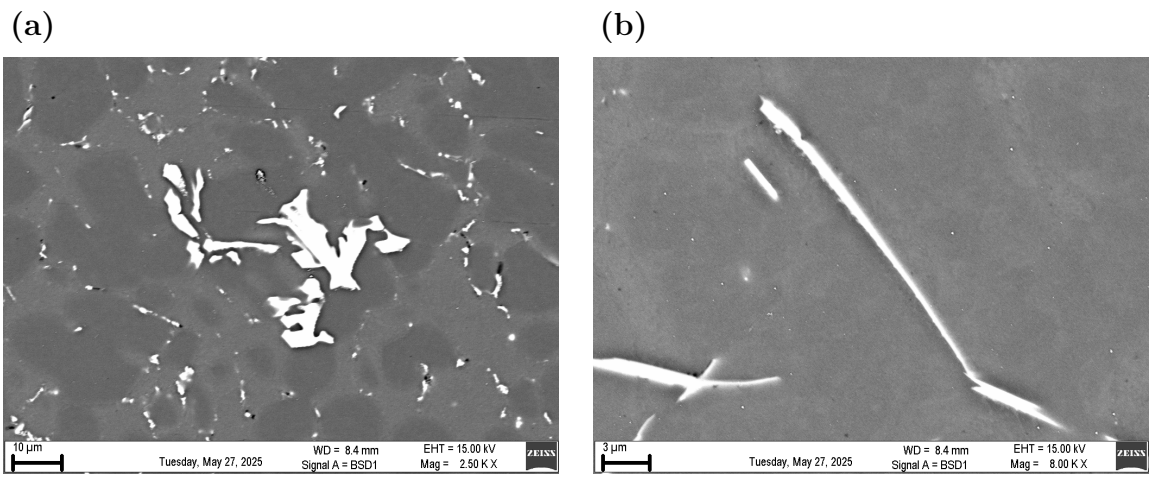

Figure 2.2: SEM images of intermetallic phases at 100 K/s cooling rate: (a) α-$Al_{15}(MnFe)_3Si_2$ morphology, (b) β-Al_5SiFe platelet morphology, note the difference in scale between the phases.

The size and morphology of IMC play an important role in determining both castability and mechanical properties. In particular, the interactions between time and temperature during solidification govern the sequence and kinetics of phase formation. Their size and morphology are further affected by the alloy composition and cooling rate, which determine whether intermetallics form before the growth of the aluminium dendritic grain network or grow freely within the liquid or concurrently with it, often leading to larger, more interconnected structures.

Phases that nucleate during the later stages of solidification are typically restricted in their growth due to the limited availability of remaining liquid and typically form finer morphologies. Conversely, early-forming phases tend to grow more extensively. In general, larger intermetallic phases are associated with detrimental effects on mechanical performance and processing characteristics [27].

Mg_2Si: In Al-Si alloys with Mg additions, two primary Mg-containing secondary phases can form, Mg_2Si and the π-phase. Mg_2Si is an intermetallic compound with an FCC crystal structure that can form when there is sufficient Si and Mg in the melt. Under equilibrium conditions, Mg_2Si tends to form around the ternary eutectic point ($\sim$555°C) along with Al and Si; however, in practice, with fast cooling conditions used in HPDC, Mg_2Si forms at the end of solidification in a non-equilibrium reaction along with other phases. The amount of Mg_2Si in castings is often low, as Mg usually resides within the aluminium matrix during high cooling rates. The Mg_2Si that forms in the as-cast microstructure often appears as small, hard precipitates with a morphology resembling script-like or chunky particles in the eutectic region. One key aspect is that during HPDC, the high cooling rate retains a supersaturated solid solution of Mg in the Al matrix; thus, the excess Mg remains available to form the Mg_2Si precipitates during heat treatment [28].

π-$Al_{18}Fe_2Mg_7Si_{10}$: The π-phase is often referred to as a complex quaternary intermetallic, containing Fe, Mg, Si, and Al. It is denoted as π-Al(Fe,Mg)Si in literature, with a nominal composition expressed as $Al_{18}Fe_2Mg_7Si_{10}$ or $Al_8FeMg_3Si_6$ in some

phase studies [29]. For the π phase to form, both Mg and Fe, containing around 5-10% Fe, tend to be hard and brittle. Under equilibrium conditions, the π-phase typically forms from a peritectic reaction at approximately 595-565°C, followed by a eutectic formation at ∼approximately 554°C. During high cooling rates in non-equilibrium cooling in the HPDC process, an invariant pattern is often observed at ∼554°C as the last phase sequence in solidification, expressed as:

$$\mathrm{L} \rightarrow \mathrm{Al} + \mathrm{Si} + \mathrm{Mg_2Si} + \pi\text{-phase}$$

This pattern suggests that in the final region of phase solidification, the liquid becomes enriched in solute elements, such as Si, Mg, and Fe. Thus, the last pocket of liquid simultaneously forms the Al matrix, Si, Mg_2Si and the π-phase, which nucleate and grow separately. This results in the π-phase typically appearing in the microstructure as constituents of the eutectic regions, often attached to other particles, such as Mg_2Si or β-$AlSiFe$. The rapid cooling in the HPDC process suppresses diffusion and causes undercooling, resulting in the π-phase forming in a finer and more dispersed manner [28].

2.2.2 Sludge factor

The likelihood of a primary Fe-rich particle, known as sludge, can be predicted by the application of the empirical sludge factor equation (SF) [30] [31]. The foundation of the SF concept is that above certain compositions and furnace temperatures, the sludge could be avoided. It has been widely used and referred to in the industry. It indicates the combined effects of Fe, Mn, and Cr; the accepted equation of SF is expressed as:

$$\textit{Sludge factor (SF)} = (1 \times \mathrm{wt.\%Fe}) + (2 \times \mathrm{wt.\%Mn}) + (3 \times \mathrm{wt.\%Cr}) \tag{2.1}$$

A more recent application of SF involves its influence on morphology, where the size and quantity of sludge depend primarily on the Fe content [32]. Some early works show that keeping the SF below ∼1.4 at typical holding temperatures of 620 (°C) can result in minor sludge formation [31]. The topic has been widely researched, with quantified effects found between the Fe:Mn:Cr ratio and sludge particle morphology. Additionally, the effects of slow cooling and low holding temperatures have a significant impact on promoting sludge formation [33]. These findings have later been used as an authoritative source behind North American Die Casting Association (NADCA) guidelines [34].

A recent study combines computational thermodynamics using CALPHAD-based Scheil solidification simulations in conjunction with experimental validation to analyse. Their research aim was to revisit the sludge factor concept from a thermodynamics perspective in Al-Si die-cast alloys by varying Fe and Mn content. They found that the β phase fraction increases linearly with Fe content and is significantly reduced with the addition of Mn; increasing Mn from 0.1 to ∼0.8 wt% notably suppresses β-AlFeSi formation. At levels above ∼0.4 wt% the β-phase precipitation

is almost entirely eliminated at low Fe concentrations at ∼0.1 wt%. At higher Fe concentrations, Mn cannot completely suppress the β-phase formation; at 0.8 wt% Mn, increasing Fe from 0.15 to 0.20 roughly doubles the amount of β-phase fraction.

Conversely, Mn promotes the formation of α-AlFeSi intermetallics. This Mn-rich α-phase can begin to solidify at a higher temperature, even before the solidification of α-Al, i.e., primary Al solidification at ∼590 °C, thus promoting the less harmful α-phase formation and delaying the emergence of β-phase. As a result, in alloys with a higher Mn content, the β-phase tends to precipitate in the final and later stages of solidification. The Scheil simulations have shown that the sludge formation essentially varies linearly with the Fe and Mn content, mirroring the empirical sludge factor presented in Equation 2.1. At the same time, the β-phase fraction exhibits a more complex, non-linear behaviour. The CALPHAD predictions align with the established sludge factor criteria at an SF of ∼1.6, with a small amount of α-phase. The primary sludge with α-phase does not form until the sludge factor exceeds 1.3. However, the SF cannot be universally applied and must satisfy the alloy-specific composition requirements, such as Cr/Fe $<$ 1 and Fe/Mn $<$ 1 for the SF to be applicable [35].

2.3 Solidification

One of the primary reasons why Al-Si alloys are used for cast alloys is due to the fact that Si is considered a "forgiving" element for foundry applications, as it compensates for aluminium. Si expands during solidification, leading to a reduction in solidification shrinkage and minimisation of pores [7]. It is widely known that solidification defects, such as gas pores, shrinkage, and oxide films, have a significant negative impact on the mechanical properties of cast aluminium alloys [8].

Among the strategies for improving performance, microstructural control during solidification is the most effective method for refining FIMC [20]. Becker et al. [25] have provided an extensive quantitative assessment of how the cooling rate governs the nucleation and growth behaviour of Fe intermetallic phases in the Al-Si-Fe-Mn alloy system for Fe contents of 0.75-1.5 wt.% and Mn contents of 0-0.75 wt.%. Their study has shown that slower cooling rates (0.05-1 K/s) favour the formation of the coarse plate-like β-Al_5FeSi intermetallics, while intermediate cooling rates (5-50 K/s) promote the transformation toward more compact α-$Al_{15}(MnFe)_3Si_2$ and finer, metastable δ-Al_3FeSi_2 phases. The α-phase varies from up to 100 μm at low cooling rates to a size of 10 μm for 200 K/s. The β-phase is nearly suppressed entirely, being replaced by the metastable δ-phase, which exhibits smaller intermetallic sizes with an estimated range of 5-20 μm for cooling rates of 50-200 K/s. This reflects the role of undercooling and limited diffusion in the formation of metastable phase formations.

The rate of β-AlFeSi intermetallic particles can be suppressed and decreased using various techniques, such as increasing the cooling rate, adding Mn, and superheating the melt. The content of Mn to neutralise the precipitation of the β-AlFeSi phase

in Al-Si alloys is strongly dependent on the cooling rate during solidification. The addition of Mn affects the thermodynamics related to the expansion of the α-AlFeSi phase formation region while reducing β-phase formation. A high cooling rate leads to a decrease in the formation temperature, to a point lower than that of the silicon eutectic formation temperature [36].

To properly understand the β-phase, it is essential to comprehend the nucleation sequence in Al-Si alloys, as this sequence enables the formation of primary α- and β-phases. The β-phase in Al-Si alloys has been reported to be formed by nucleating along the nucleation of the double oxide layer film. The film induces surface turbulence as it reacts during the pouring and casting processes. The inner side of the oxide film is dry and unbound, as air is trapped inside, while the other side is in contact with the unsolidified molten alloy and is, therefore, the only possible nucleation site for the β-AlFeSi phase. Further outlining the relationship between nucleation sites in Al-Si-Mg alloys reveals that oxide layers can serve as nucleation substrates for all AlFeSi phases [37, 38].

The solidification rate has a significant influence on the SDAS, with higher cooling rates resulting in a more refined microstructure and reduced SDAS. This refinement enhances key mechanical properties, such as yield strength, tensile strength, elongation, and fatigue resistance [8]. While alloying elements may play a secondary role, there is an inherent relationship between dendritic refinement and the cooling rate itself, which directly decreases the SDAS and promotes a finer microstructure and morphology [6].

2.3.1 Secondary dendritic arm spacing

There are two types of dendritic growth: the first is columnar growth, which is driven by the unidirectional displacement of the isotherms that occurs at the mould walls. The other is equiaxed dendrites growing from the nuclei in the undercooled melt; the local undercooling determines their growth, ΔT. If a thermocouple is placed at a fixed position in the melt and is overgrown by the dendrites during solidification, different cooling curves could be recorded for directional and equiaxed growth. This is essential to note as it affects the nucleation of equiaxed dendrites. Additionally, due to microsegregation, some eutectics will typically form during the later stages of solidification. For directional growth, the dendrites are in contact with the mould wall, which acts as a heat conductor, transferring the heat in the opposite direction to their growth. As the melt is the hottest part of the system, it affects the growth of equiaxed dendrites, where the heat is produced during solidification and must be transported through the melt [39].

Secondary dendritic growth can be described as a type of "sinusoidal perturbation". When a planar solid/liquid interface becomes unstable, these perturbations begin to grow and eliminate their smaller neighbours until they finally become secondary dendrites and continue to grow perpendicular to the primary trunk. These secondary arms will continue to grow and eliminate the smaller branches, provided that their

length is less than half the radius of the primary dendrites. When their field of diffusion comes in contact with neighbouring dendrites, they slow down and eventually cease to grow. Over time, a ripening process causes the branched structure to transform into a coarser, less branched, and more widely spaced structure. This process is analogous to the Ostwald ripening (dendrite arm coarsening) of precipitates. A schematic representation is shown in Figure 2.3, where a thin secondary arm melts, resulting in a doubling of the local spacing. The driving force behind the ripening process is the difference in chemical potential among crystals with varying interfacial energies, which arises from differences in their curvatures [39].

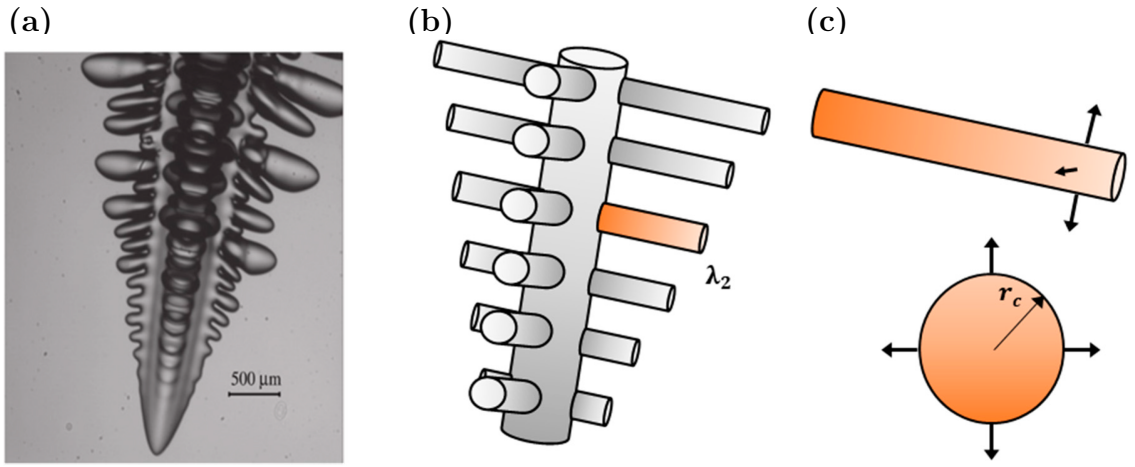

Figure 2.3: Schematic representation of the dendrite side branches simplified as cylinders, illustrating factors affecting coarsening. a) Real dendrite image, b) schematic of side arms simplified as cylinders, c) front and side view of a single dendrite arm. Adapted from [40], licensed under CC BY 4.0. DEED. Licence: `https://creativecommons.org/licenses/by/4.0/`

During solidification, oxides are pushed ahead of growing dendrites into the interdendritic and boundary regions; this is an important mechanism for cast alloys such as Al-Si that have solid surface films. Oxide formation on the surface of aluminium is an inherent property of aluminium, as it serves as a protective film over the liquid. Their entrapment can be avoided by altering or redesigning the casting production process, mainly by minimising the pouring and disturbance of the liquid metal surface [7].

It is worth noting that while vacuum casting can reduce the formation of oxides, it cannot entirely prevent their presence. One of the primary sources of mechanical weakening in liquid aluminium is the formation of inclusions, specifically bifilms. These are entrained into the bulk liquid when surface oxide films are folded over during processing and pouring. Such bifilms, essentially double-layered oxide films, act as extrinsic defects and can lead to pore formation while circumventing the nucleation process. This mechanism is also associated with hot-tearing during the solidification process. These folded oxide films in the melt have two distinct sides: the dry, unbounded inner surface and the wetted exterior surface, which is in contact with the melt. The outer wetted interface of these oxide films serves as a preferred

substrate for the nucleation of certain Fe-rich phases in Al alloys [11, 37].

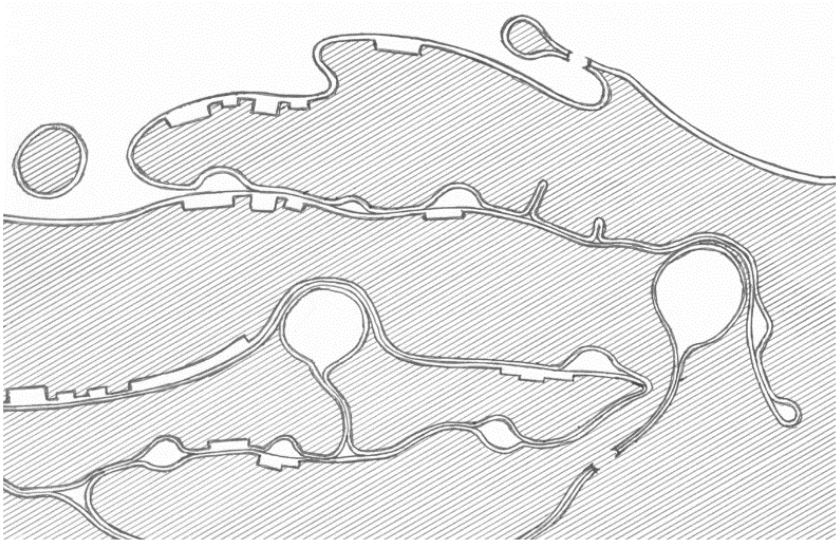

Figure 2.4: Bifilms and gas bubbles, caused by turbulence in the melt. Adapted from [41] as per free use by Open Access. Licence: https://www.mdpi.com/openaccess.

One proposed view of the relationship between dendrite arm spacing and elongation to failure of cast alloys is that an increased dendritic arm spacing results in a decrease in ductility. A theory by J. Campbell for this pattern suggests that it is the result of the unfurling of bifilms. If the solidification of the melt is rapid, the bifilms are frozen as a compact, small and relatively harmless defect. While longer solidification time, this unfurling process can progress further, leading to larger crack-like defects [42].

In Al alloys, the growth of secondary dendrites is significantly influenced by the heat extraction rate, which governs the solidification kinetics during the casting process. An empirical logarithmic relationship exists in which SDAS is inversely proportional to the solidification rate. This relationship is characterised by an alloy-specific exponent constant denoted as "n" for aluminium alloys, with reported values of "n ranging between 0.2 and 0.5 [43, 44].

In cast materials, SDAS is a key indicator of microstructural refinement and has been shown to affect both tensile strength and ductility directly. These properties exhibit an inverse relationship with dendrite arm spacing, where finer SDAS generally corresponds to improved strength and elongation. Furthermore, in cast alloys subjected to secondary processing like heat treatment, micro-segregation associated with dendrite solidification can compromise the chemical homogeneity. These secondary processing techniques sequentially affect the distribution and morphology of secondary phase particles, both of which are critical factors in determining the overall mechanical performance of the material [45].

In addition to the alloy composition, the heat extraction rate is a critical factor influencing the microstructure development, especially in conjunction with the solidification time or equivalent cooling rate [45]. The SDAS can be related to the solidification rate or the cooling rate using the following equations:

$$\lambda = A(t_s)^n \tag{2.2}$$

$$\lambda = B\dot{T}^{-n} \tag{2.3}$$

where λ is the secondary dendrite arm spacing (µm), t_s is the solidification time (s) and $\dot{T}$ is the cooling rate during solidification ($^{\circ}\mathrm{C\,s^{-1}}$) which is defined using the following equation:

$$\dot{T} = \frac{\Delta T}{t_s} \tag{2.4}$$

For a given n value and a known ΔT, A can be calculated using the equation:

$$A = \frac{B}{\Delta T^n} \tag{2.5}$$

The values for n and A or B are typically derived empirically from experiments where the measured secondary dendrite arm spacing is compared to the solidification time or cooling rate [45].

2.4 Computational thermodynamics - Scheil simulations

The Al-Fe-Mn-Si quaternary system is of considerable industrial relevance for HPDC alloys and other applications that utilise recycled aluminium. These alloying elements/impurities interactions govern the solidification path and the final microstructure. In recent years, reliable phase equilibrium data are now available as a result of advanced thermodynamic assessments and CALPHAD modeling, which enables simulations of both equilibrium and non-equilibrium (Scheil-type) solidification paths [46].

The classic Scheil-Gulliver equation describes the solidification behaviour of alloys under non-equilibrium conditions, based on the assumptions of: no diffusion in the solid phase, perfect mixing in the liquid phase and local equilibrium at the solid-liquid interface. Equation (2.7) shows the solute concentration in the solid phase (C_S) as a function of the solid fraction (f_S) as described by:

$$C_S = C_0\, k\, (1 - f_S)^{(k-1)} \tag{2.6}$$

Where:

- C_S is the solute concentration in the solid at a given solid fraction f_S,

- C_0 is the initial solute concentration in the alloy,
- $k = \frac{C_S}{C_L}$ is the equilibrium partition coefficient (ratio of solid to liquid solute concentration at the S/L interface),
- f_S is the fraction of solid formed during solidification.

A schematic illustration can be seen in Figure 2.5. The equation is used as a tool to predict micro-segregation in solidifying alloys and is widely used in computational simulations, such as Thermo-Calc [47].

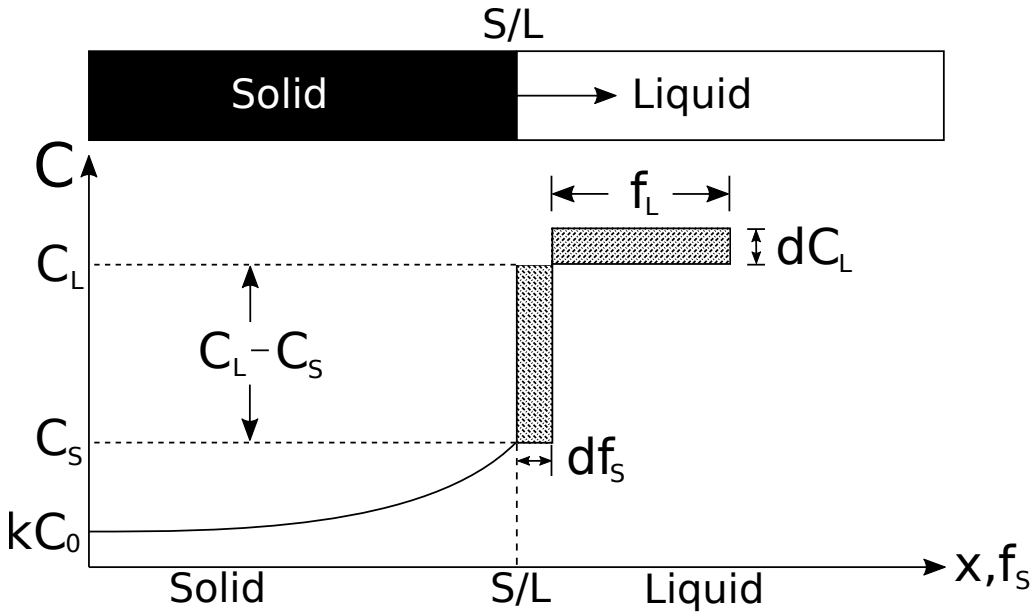

Figure 2.5: Illustration of the Scheil solidification equation.

One of the downsides of applying the Scheil-Gulliver model arises from its simplification. There are several accounts where the formation of FIMC phases deviates from the observations from the experiments. An example from Becker et al. [25] showed the formation of δ-Al_4FeSi_2, rather than the predicted β-Al_5SiFe phase, and, in another case, the appearance of α-Al_8Fe_2Si where β-Al_5SiFe had been expected. These discrepancies are thought to be attributed to assumptions applied by the Scheil–Gulliver model, which suggests that the role of kinetic nucleation in the phase formation is negligible [21].

In an article by Erik Granhed et al., the formation of α-$AlFeSi$ sludge in AlSi10Mg was investigated by applying computational thermodynamics based on the CALPHAD method. They found that the β-fraction increases linearly with increasing Fe content, and the well-defined slope is based on the concentration of Fe between 0.1 and 0.4, and Mn between 0.1 and 0.8, with steps of 0.05. Granhed did not find a relationship between the β fraction and the content of Mn, either linear or logarith-

mic. The exponent for the slope varied between 0.3 to 1.2 between the investigated intervals. For low concentrations of Fe (∼0.1 wt%) a content of ∼0.8 Mn is enough to suppress the formation of β-$AlFeSi$ completely; however, that is not the case at higher concentrations of Fe [35].

Solute Trapping: Solute trapping is a non-equilibrium phenomenon which occurs during rapid solidification when the separation of solute elements in a liquid-solid interface is suppressed due to high interface velocities. For equilibrium conditions, solute partitioning is guided by the equilibrium partition coefficient mentioned previously, defined as:

$$k_e = \frac{C_S}{C_L} \tag{2.7}$$

where C_S and C_L are the solute concentrations in the liquid and solid phases, respectively. When the solidification velocity increases, the actual coefficient $k(V)$ begins to deviate from k_e as described by the Continuous Growth Model (CGM), which introduces a velocity-dependent partition coefficient with a modified liquidus slope accounting for kinetic effects at the interface [48].

In a study by Mohammed et al., which examined alloys with similar compositions to this work within the Al-Si-Fe-Mn alloy system, it was reported that the resulting microstructure consisted predominantly of dendritic morphologies. Their work suggested that the effect of solute trapping was negligible. They observed that, even though non-classical Scheil-Gulliver models, including velocity-dependent partition coefficients, are key to predicting solute segregation in extremely rapid solidification processes such as additive manufacturing or welding, these models showed no noteworthy difference in their predictions compared to classical Scheil simulations for their alloy system. They concluded that classical Scheil calculations provided reliable solute segregation estimates under their experimental conditions, and their discrepancies between predicted and observed FIMC phases were expected to be attributed to phase formation kinetics rather than solute trapping effects [21].

3
Methods

The alloy system prepared and researched is based on the Al-Si-Fe-Mn system in the Al-rich corner, with small additions of Mg. Fe and Mn are the prime variables. The compositional range investigated is presented in Table 3.1, with Al as balance. Throughout the investigation, Mg is maintained at a low level of 0.1-0.2 wt% to reflect typical levels in secondary die-cast alloys and to avoid excessive amounts of Mg_2Si, thereby not overshadowing Fe-intermetallics, which is the primary focus of this thesis. Silicon is varied at 8.0-9.5 wt% to examine a slight shift towards or away from the eutectic region. Mn and Fe each varied from 0.1-1.2 wt%.

These compositional variations yield a grid of 300 possible compositions - not all will be cast, but all the compositions will be simulated. The compositions simulated are summarised and named in Appendix A. Some additional compositions were also investigated and added in Appendix A.10. These compositions will not be used for investigating the Al-Si-Fe-Mn system, but rather focus on the Scheil solidification paths.

Table 3.1: The alloy composition range investigated, in wt.% (Al as balance).

	Si	**Mg**	**Mn**	**Fe**
Min	8.0	0.1	0.10	0.10
Max	9.5	0.2	1.20	1.20
Step size	0.5	0.05	0.30	0.30

For the experimental part of the thesis, cast samples from a total of 11 different ingot alloys were provided, and then arc-melted, produced, and examined for this work. The composition ranges of the alloys are shown in Table 3.2. Only one of the alloys came from a primary source; the rest of the alloys were derived from secondary sources with a recycled content (RC) of up to 95%.

Table 3.2: Chemical composition range of cast alloys investigated in wt.%

Si	**Fe**	**Mn**	**Mg**	**Other**	**Al**	**RC (%)**
8.0–10	0.10–0.50	0.10–0.70	0.10–0.40	<0.20	Balance	35–95

Some of the characteristics of the alloys studied are presented in Table 3.3, providing an indication of their compositions.

Table 3.3: Characteristics for alloys studied in this work.

Alloy	Si	Fe	Mn	Mg	RC (%)
A1	↓	↓	↑	–	10-20
A4	↑	↑	↓	↑	>70
A6	↓	↓	↑	↑	>70
A11	↓	↓	↑	–	>35

3.1 Sample preparation

The alloy preparation was carried out using industry-provided ingots with varied recycled content and mixtures thereof. A total of 11 different alloys were produced using arc melting. Each alloy was cut from the provided ingot alloy to be melted in an arc furnace under argon and cast into a copper chill mould, resulting in a cooling rate of 100 K/s to simulate the high cooling rates of HPDC. The melt can reach temperatures above 2000 K [12], the arc melter can be seen in Figure 3.1. The mold had an outer diameter of 50 mm and a height of 150 mm. The inner dimension consisted of 10x10 mm with a height of 90 mm, resulting in a cast cuboidal sample. The samples were then cut into two different specimens, with the dimensions 10x5 mm, one from the top and the other from the bottom part of the cast sample.

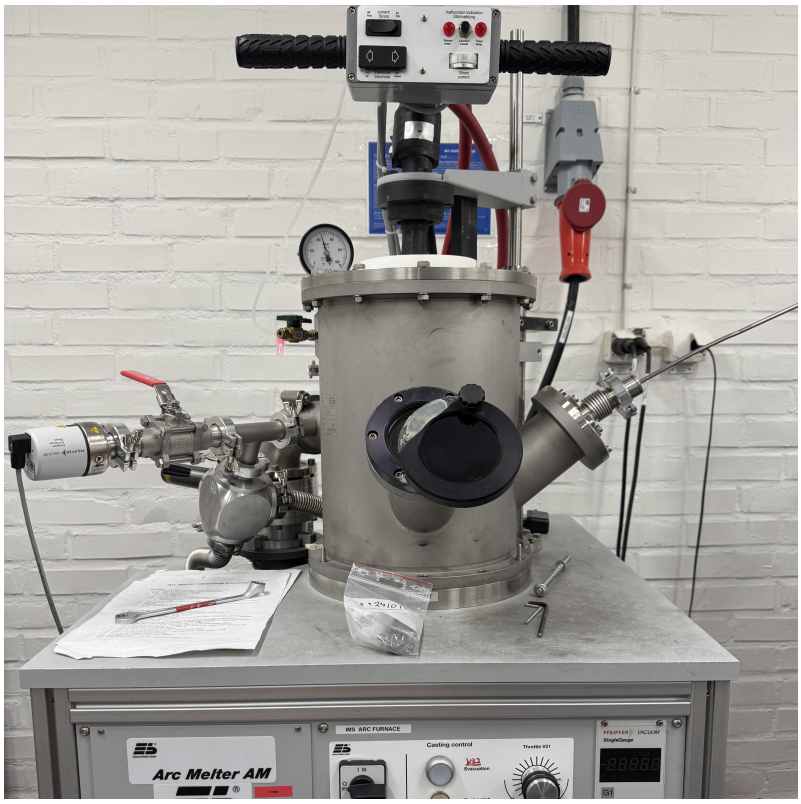

Figure 3.1: Arc melter used for casting.

The holder for the cast specimens was created using additive manufacturing (AM); the 3D model is shown in Figure 3.2 to facilitate a high-throughput methodology for the project.
Aluminium specimens were cold-mounted to avoid exposing the specimen to elevated temperatures, which could alter the microstructure. To ensure electrical conductivity during SEM analysis, a copper wire was affixed to the rear side of each sample. The integration of the conductive wire in this fashion allows the samples to be used interchangeably between different experimental methods, adapting a high-throughput methodology. If the conductivity of the copper wire was not sufficient, gold sputtering was employed on the sample. The holder for the specimens is shown in Figure 3.2, and can accommodate a total of eight specimens to be mounted per sample holder.

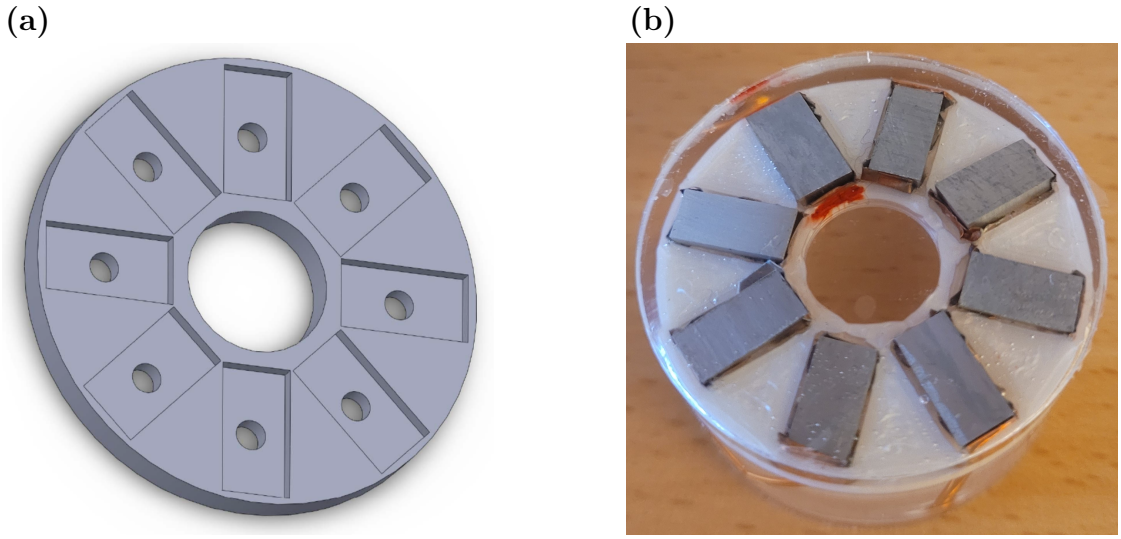

Figure 3.2: Sample-holder for cast specimens: (a) 3D model produced using additive manufacturing, (b) cast samples in a manufactured custom holder.

The preparation for the specimens was done by following these steps:

1. The specimens were ground using 320 grit SiC paper by hand, and grinding continued until the specimen surfaces were co-planar and cutting damage was removed. After grinding, the specimens were rinsed and dried.
2. The specimens were then ground using a 9-μm MD-Dur silk cloth. Complementary rotation was used. Specimens were polished for 4 minutes using 9-μm diamond polish, with an applied load of 30 N per specimen, refreshed with one drop every 5 seconds. After polishing, the specimens and holder were cleaned using water and soap solution, rinsed with water and isopropanol, and then dried.
3. The polishing continued with a 3-μm diamond on an MD-Dac or MD-Mol acetate pad using the same conditions as step 2. After visual inspection, an additional step may be performed if deemed necessary.
4. The final polishing step used OP-S or OP-U colloidal silica on an MD-Chem pad for 90 seconds, followed by 60 seconds with water under a 15 N load per

specimen. Contra-rotation was used with a rotation of 100 rpm. Cleaning was done as described in step 2 with the addition of ultrasonic cleaning.

After arc-melting of the samples, optical emission spectroscopy (OES) measurements were performed on some of the cast samples. OES analysis showed Al evaporation of up to 10%, while Mg losses reached 20%. These elemental reductions are likely a consequence of elevated temperatures involved in arc melting, which promote evaporation and may require further investigation. Due to Al loss, the Si content increased by approximately 10%, while the concentration of other elements remained largely stable.

3.2 Measurement of secondary dendritic arm spacing

There are several ways to measure the SDAS; if they are in an ordered arrangement, the "secondary arm method" or "linear intercept method" can be applied. A schematic representation is shown in Figure 3.3. To get an accurate measurement, the dendritic arms measured need to be 30 or more, while the minimum amount of dendritic arms should comprise 3 or more. The equation are as follows:

$$\lambda_2 = \frac{\left(\frac{l_1}{n_1-1} + \frac{l_2}{n_2-1} + \cdots + \frac{l_m}{n_m-1}\right)}{m} = \frac{\left(\sum \frac{l_i}{n_i-1}\right)}{m} \tag{3.1}$$

Where λ_2 = dendrite arm spacing in μm, l_i = distance from arm group boundary to the boundary of ordered dendrite arms to be measured, n_i = number of intersections between the boundary of ordered arm groups to be measured and the arm boundary, which is drawn from the group boundary, $(n-1)$ = number of dendrite arms, and m = number of dendrite arm groups measured [44].

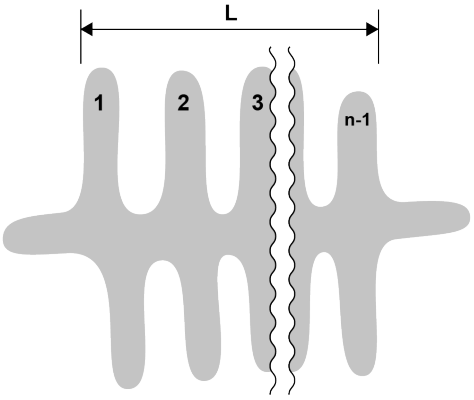

Figure 3.3: Schematic illustration of the measurement of SDAS using the linear intercept method.

Images of the microstructure of the alloys were taken using stereo optical microscopy (SOM) and analysed and measured for SDAS manually using ImageJ software.

3.3 Scanning electron microscopy

Understanding the visual presentation in the images produced by scanning electron microscopy (SEM) is an integral part in metallurgical sample analysis. SEM imaging is done by the interactions between an electron beam and the sample material, which can be used for different purposes based on the signal used. A higher acceleration voltage allows for the electrons to penetrate deeper into the surface, which may enhance the BSE signal strength and the contrast for the atomic numbers. The contrast in SEM imaging is influenced by several factors, such as:

Secondary Electrons: These are produced from the sample surface from *inelastic* scattering of the primary beam electrons. The SE imaging highlights typographical contrasts and variations, such as surface features and textures. The elemental composition is not reflected to a large extent, especially compared to BSE.

Backscattered Electrons: The resulting image from BSE imaging arises from the elastic scattering of primary electrons. This produces compositional contrast, as heavier elements (with higher atomic numbers) scatter more electrons back to the detector than lighter elements, which scatter fewer. This results in a contrast difference, where heavier elements appear brighter compared to lighter elements, which appear darker in the image. An example would be an Fe-rich intermetallic with the atomic number 26, compared to a Si-rich intermetallic with the atomic number 14, where Fe will appear brighter in BSE imaging.

Energy-Dispersive X-ray Spectroscopy: For the proper identification and quantification of elemental compositions of the phases to be observed, EDS was employed. EDS is based on the detection of elemental characteristic X-rays emitted from the sample surface with a focused electron beam. The X-ray energy spectrum is then applied for elemental identification of a semi-quantitative composition analysis. While BSE will provide morphological observations and phase contrasts, EDS point analysis and mapping were employed to identify and distinguish Fe-rich, Mn-rich, Mg-containing, and Si-containing phases. The results were used for phase identification and comparison in conjunction with the thermodynamic predictions from Scheil simulations.

Electron backscatter diffraction: The application of EBSD lies outside of the scope of this thesis; therefore, crystallographic phase mapping and grain orientation analysis were not performed. However, a proper understanding of this technique is an integral part of microstructure analysis, as it involves examining crystallographic features such as phase distribution and grain orientation. Bragg's law is a simplified model to understand the conditions required for optimal diffraction of X-rays by a crystalline material, given by Equation 3.2:

$$n\lambda = 2dsin\theta \tag{3.2}$$

Where λ is the wavelength of the incident, d is the spacing between crystal planes, θ is the incident angle, and n is the order of diffraction. EBSD relies on the principle to generate Kikuchi patterns, which allow for the mapping of crystal orientations and identification of distinct phases. In Figure 3.4, the diffraction of X-rays by crystal lattice planes is illustrated, demonstrating the geometric principle of Bragg's law. The path difference between the X-rays reflected from adjacent lattices must be an integral multiple of the wavelength for the diffraction conditions to be met.

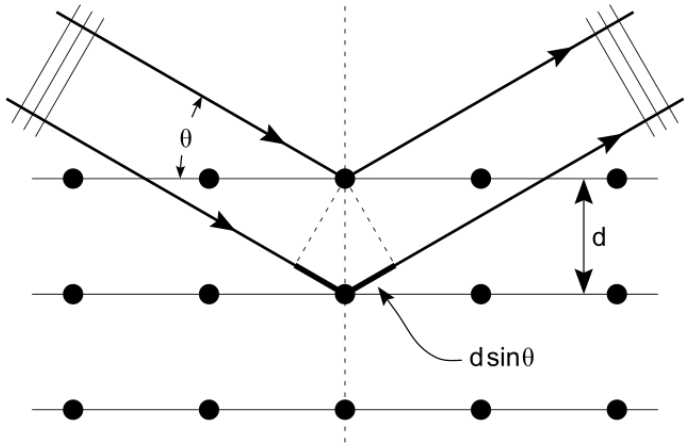

Figure 3.4: Bragg diffraction diagram illustrating constructive interference of X-rays scattered by crystal planes. Adapted from [49] as per CC BY-SA 3.0 DEED. Licence: https://creativecommons.org/licenses/by-sa/3.0/

3.4 Scheil simulations

To simulate the solidification behaviour and phase transformation in Al-Si-Fe-Mn alloys (with small additions of Mg) under conditions similar to HPDC and arc melting, the Scheil-Gulliver solidification model was used, incorporating back-diffusion, with Thermo-Calc version 2025a and the TCAL9 database. The Scheil model assumes infinitely fast diffusion in the liquid phase and no diffusion in the solid phase. However, using the model with back-diffusion allows for limited diffusion for the primary phase of the solid material. By using the diffusivity data from the MOBAL8 database, the calculations account for the back diffusion of all elements into the aluminium matrix (FFC) phase. This simplification and assumptions in the Scheil model give a more conservative prediction when it comes to segregation, which is crucial for understanding the formation of different phases [11, 47].

In Table 3.4, the phases thought plausible to appear within our system are summarised, showing their name commonly referred to in literature, their stoichiometric compositions, along with the labelling used in Thermo-Calc and the labelling from which this work will refer from this point. The simulations were performed with a temperature step size of 0.1°C to ensure high resolution of the calculation results.

The cooling rate of 100 K/s was chosen to reflect the high cooling rates of both arc melting and the typical high cooling rates of HPDC processes.

Furthermore, the simulations will be compared to the cast samples prepared for the experimental analysis, which are cast with the same cooling rate of 100 K/s. Thermo-Calc requires a value for the expression of secondary dendritic arm spacing using either the power law as seen in Equation 2.3, where the values of "B" and "n" are given by the user (denoted "C" and "n" in Thermo-Calc) or a constant value given by the user. For this work, the constant value for the SDAS will be taken from the results described in section 3.2, which will directly connect the experimental specimens to the simulations. Additionally, back diffusion was taken into account, although its effects are considered negligible due to the high cooling rate used in this study.

For this work, the solute trapping model was not applied for the following reasons:

1. The Al-Si-Fe-Mn system consists solely of substitutional elements, where diffusion generally is slower, and the trapping effects are less pronounced at cooling rates of 100 K/s.
2. The Scheil-Gulliver model assumes no diffusion in the solid and complete mixing in the liquid phase. This leads to a prediction of maximum possible segregation, providing a conservative upper-bound estimate by neglecting solute trapping kinetics that would otherwise reduce segregation.
3. The interface velocities simulations and experiments are moderate and do not reach the threshold for the trapping regime (below 1 m/s). At these velocities, solute atoms still have time to redistribute according to equilibrium partitioning, and solute trapping is negligible. Rather, some limited diffusion will be approximated, taking back-diffusion into account.

Table 3.4: Phases, stoichiometric compositions and Thermo-Calc (TCAL9) identifiers.

Phase	**stoichiometry**	**Phase Naming**	
		Thermo-Calc (TCAL9)	**This Work**
L	Liquid	LIQUID	L
Al	Al Matrix	FCC_A1	α-Al
Si	Si diamond	DIAMOND_A4	Si
τ_4 or δ	Al_3FeSi_2	AL3MNSI2	δ
τ_5 or α'	Al_8Fe_2Si	AL8FE2SI	α'
τ_6 or β	Al_5FeSi	AL9FE2SI2	β
τ_9 or α	$Al_{15}(Fe,Mn)_3Si_2$	AL15SI2M4	α
π	$Al_{18}Fe_2Mg_7Si_{10}$	AL18FE2MG7SI10	π
Mg_2Si	Mg_2Si	MG2SI_C1	Mg_2Si

4

Results and discussion

This chapter presents the results from both the experimental characterisation and the thermodynamic simulations, following a discussion of the implications of the alloying effects using recycled aluminium. The focus lay on understanding how varying concentrations of Fe, Mn, Si, and Mg influence the formation of intermetallic phases under different compositional conditions. Particular attention is given to the suppression of the β-phase, the promotion of the more benign α-phase and their solidification behaviour in relation to the Fe/Mn ratio. The predictions from Scheil-Gulliver simulations are validated experimentally through microstructure analysis to observe and consider kinetic effects and deviations. This chapter also addresses the measurements of SDAS as a key microstructural parameter, the results of which will be used as constant in the Scheil simulations.

4.1 Measured SDAS values and input parameter selection

We measured four of the 11 alloys to cover as broad a compositional range as possible for SDAS analysis; Table 4.1 summarises the measurement results. We observed slight variations in SDAS across the alloy composition. This aligns with the literature, which reports values between 10 and 25 μm for high cooling rates. For the simplification of the simulations, we decided to use the same constant in all simulations, specifically the value of A11, as it had the largest measurement pool. Figure 4.1 shows the measurement of the SDAS for A6, where only the most clear and aligned dendrites were measured. The different measurements illustrate that some interpretation is required when selecting dendrites for measuring SDAS.

Table 4.1: Measured secondary dendritic arm spacing from cast alloys.

Alloy	**Arms groups measured**	**Standard deviation**	**SDAS [μm]**
A1	31	1.173	11.83 ± 0.41
A4	32	1.539	12.43 ± 0.53
A6	36	1.653	12.52 ± 0.54
A11	53	1.326	10.68 ± 0.36

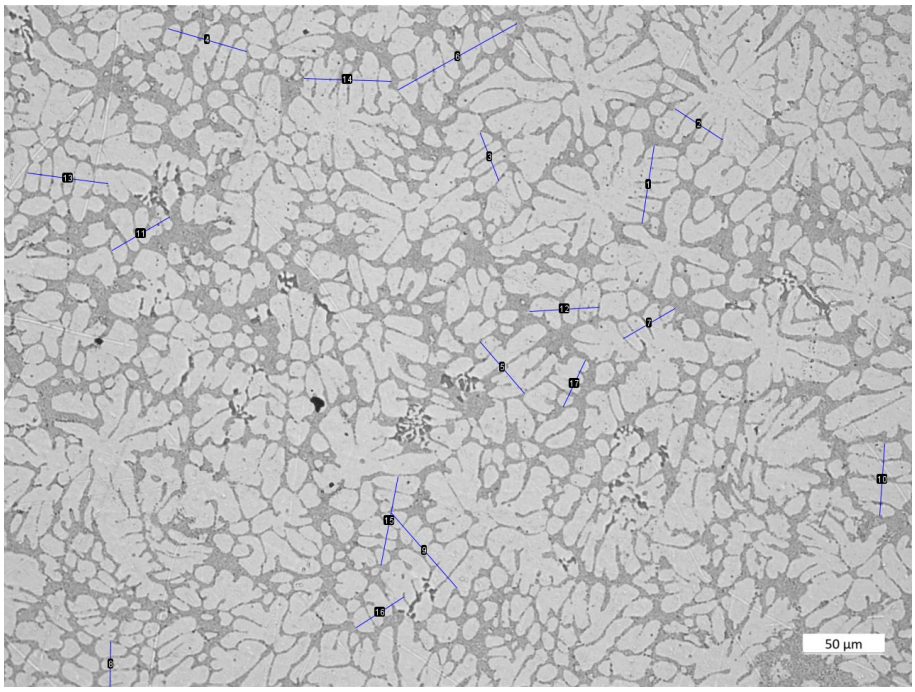

Figure 4.1: Measurement of secondary dendritic arm spacing.

4.2 Scheil simulations and correlation with experimental observations

The Scheil simulation results reveal several overarching trends. When Si, Fe, and Mg contents are held constant, increasing Mn shifts the onset of the α phase to an earlier stage in the solidification sequence: initially before the Si eutectic and at higher Mn levels, even before the formation of primary α-Al. An increase in Mn may consequently delay the formation of the β-phase. At high Mn levels, α intermetallics may form before the primary α-Al matrix, significantly altering the solidification path and increasing the overall solidification onset temperature.

In contrast to Mn, increasing Fe content has the opposite effect on the solidification sequence. It promotes the formation of β-phase, which typically occurs in the final stages of solidification. However, at high Fe contents and elevated Fe/Mn ratios, the onset of β formation may shift to higher temperatures. In general, this makes the eutectic region a playground for the formation of the β-phase.

Silicon introduces yet another dimension to the solidification process. As the primary alloying element in the Al-Si-Fe-Mn system, it allows for broad compositional variation. In this work, all alloys remain within the hypoeutectic range. Increasing Si content lowers the onset temperature of solidification. It expands the eutectic solidification region during the final solidification stages, in which multiple phases, including α-Al, Si, and intermetallics, form simultaneously.

Magnesium, while less dominant than Fe, Mn, or Si, still plays a distinct role. It has

a comparatively minor influence on the early solidification path. It slightly lowers the onset temperature, but its primary role emerges near the end of solidification, where it contributes to the formation of π and Mg_2Si phases alongside eutectic reactions. The combined effects of varying Fe/Mn ratios and Si content are visualised in Figure 4.2. This figure illustrates the influence of the Fe/Mn ratio and its corresponding influence on phase fractions as a function of varying Si content, summarised in Table 4.2.

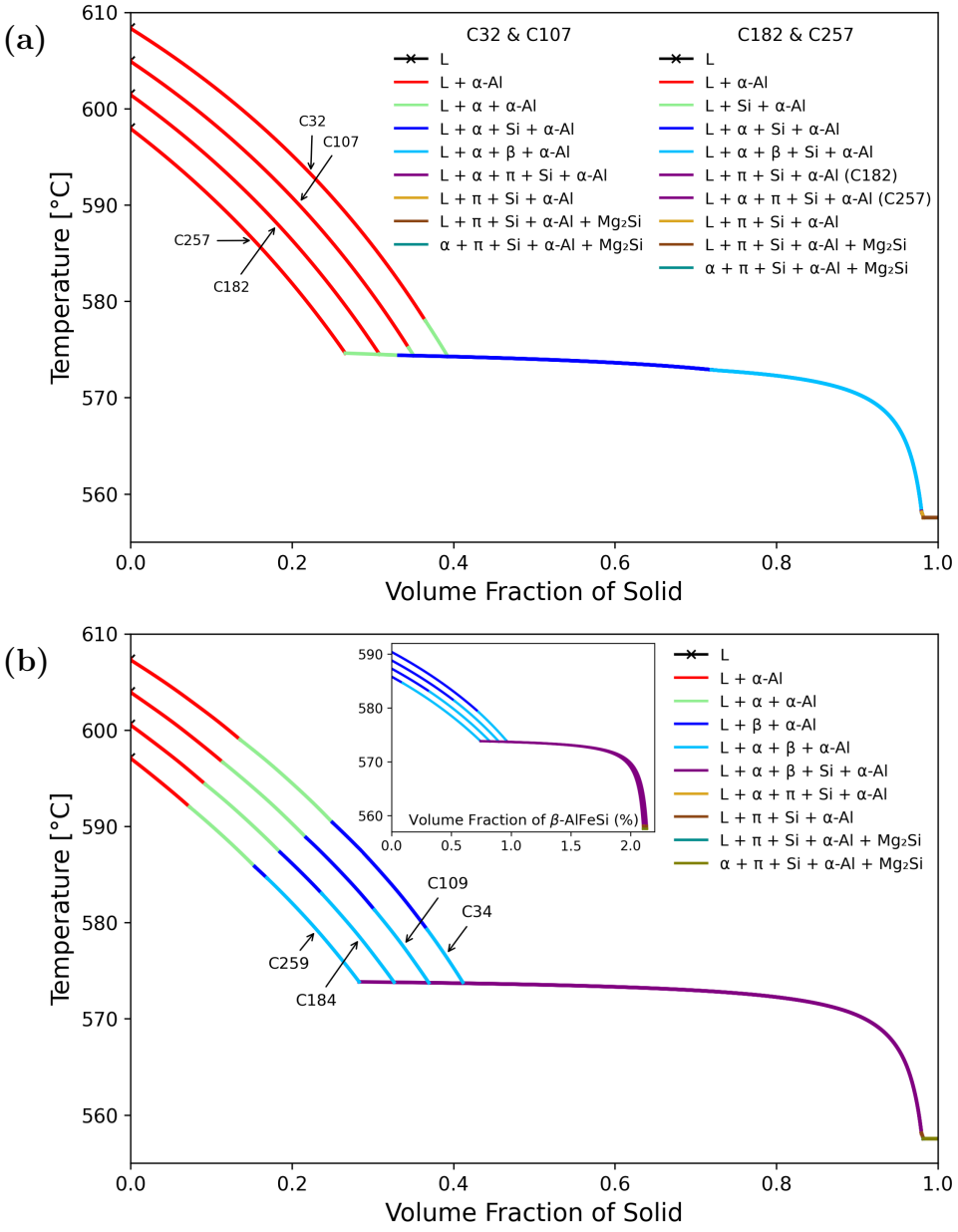

Figure 4.2: Scheil solidification curves with increasing Si content: (a) Compositions C32, C107, C182 and C257 with a Fe/Mn ratio of 1, (b) Compositions C34, C109, C184 and C259 with a Fe/Mn ratio of 3.

Notably, we can observe the effect of Si on the onset temperatures, which narrows the temperature span. As the Si content increases, the onset temperature for the

system to begin solidifying decreases; consequently, the curve enters the multiphase eutectic reaction region with a smaller fraction of solidified phases. Furthermore, in Figure 4.2 (a), we can see that Si affects the solidification path, where an increased Si content suppresses the formation of α-Al by causing the Si-eutectic region to form earlier in the solidification process.

Finally, the Fe/Mn ratio itself plays a pivotal role in intermetallic phase evolution. At a low ratio of 0.33, Mn effectively substitutes Fe in intermetallic formation by suppressing the formation of the brittle and acicular β-phase. As the Fe/Mn ratio increases, the β-phase fraction grows. However, a slight increase in α also occurs because some Mn is drawn out of the α-Al matrix, as this is thermodynamically more favourable.

By comparing these observations from the Scheil solidification curve with the experimental observations shown in Figure 4.3, and referring to the compositional data in Table 3.3, a consistent interpretation can be made.

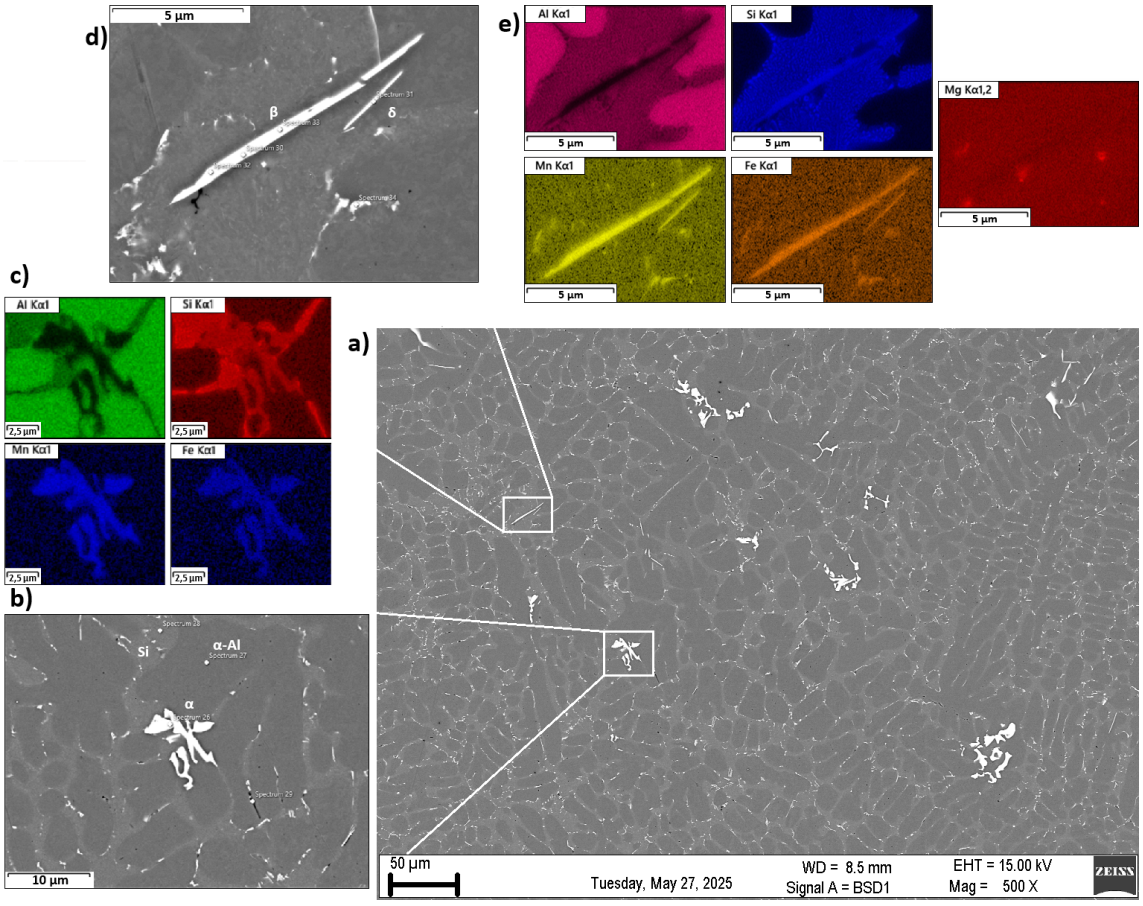

Figure 4.3: SEM-EDS mapping of sample A1, showing α, β and δ Intermetallics: (a) SEM image of the microstructure, (b) Point map of α-phase, (c) EDS mapping of Al, Si, Mn and Fe for α-phase, (d) Point map of β- and δ-phase, (e) EDS mapping of Al, Si, Mn and Fe for β- and δ-phase.

The microstructure in Figure 4.3 appears evenly distributed, with intermetallic phases primarily consisting of α-phase IMC exhibiting a compact, Chinese-script morphology. These are located between the α-Al dendrite arms, while occasional needle-shaped β-phase intermetallics are observed within the Si-eutectic region. This indicates that the α-phase either nucleates before or alongside the α-Al matrix and has been "pushed" when the dendrites grow, while the β-phase has been pressed into the Si-eutectic solution and later has formed alongside it, similar to what we saw in Figure 4.2 (a). This can also be observed from the volume fraction and the size of the intermetallics, where the α intermetallics are larger in both size and volume, ranging from 10 to 50 μm, while the β-phase ranges between 5 and 25 μm.

Notably some small intermetallics in the 1-μm range appear to adhere and nucleate from the α-Al matrix, which, judging by their size and location, indicates that these form after all the liquid has solidified, following the reaction: α+π+Si+α-Al+Mg_2Si.

Table 4.2: Calculated intermetallic phase fractions with increasing Si.

Alloy	**Onset Temperature (°C)**		**Volume Fraction** [%]		
	α-Onset	**β-Onset**	α	β	**FIMC**
Fe/Mn ratio = 0.33					
C31	574.6	569.0	0.60	0.10	0.70
C106	574.6	568.9	0.61	0.10	0.71
C181	574.6	568.9	0.61	0.10	0.71
C256	574.6	568.9	0.61	0.10	0.71
Fe/Mn ratio = 1					
C32	578.0	572.9	0.78	0.49	1.27
C107	575.2	572.9	0.79	0.48	1.27
C182	574.4	572.9	0.79	0.48	1.28
C257	574.4	572.9	0.80	0.48	1.28
Fe/Mn ratio = 3					
C34	599.0	590.4	0.89	2.10	2.99
C109	596.7	588.8	0.88	2.12	3.00
C184	594.4	587.3	0.87	2.13	3.00
C259	592.0	585.8	0.87	2.13	3.00
Constant values: Mn = 0.3 wt%, Mg = 0.15 wt%					

The EDS mapping reveals the relative difference in elemental compositions for the investigated phases. In the case of α-Al, the intermetallic region appears relatively depleted in contrast. As shown in 3.4, the aluminium matrix consists almost entirely of aluminium, while the Si-eutectic region displays a higher Si signal, which is consistent with the expected result. In comparison, the intermetallic phases exhibit a noticeably lower aluminium contrast. Additionally, EDS mapping of the α- and β-intermetallics shows a higher contrast from Mn than Fe in both phases. As we

know, Mn and Fe can be substituted interchangeably within the atomic structure; thus, we can conclude that A1 has a lower Fe/Mn ratio.

Additionally, EDS mapping reveals small, rounded features with a strong Mg signal. When comparing regions with a high Mg contrast to the corresponding Si map, an elevated Si signal is also observed in the same areas. Based on the morphology and the elemental distribution in the EDS maps, it is reasonable to infer that these features may correspond to Mg_2Si particles. Based on the knowledge we have observed from the solidification curves in Figure 4.2, we can conclude, from the microstructure, that A1 exhibits a greater relation to the solidification curves of C32 or C107 in the former figure, which is consistent with what we also see in Table 3.3.

These observations give a good indication that the solidification sequence has a significant impact on the final microstructure of the samples. Looking at the solidification curves of Figure 4.2, we observe that all solidification events occur earlier at higher Fe/Mn ratios. However, the final β-fraction remains unaffected mainly, as presented in Table 4.2. Figure 4.2 (b) (upper centre) shows the increase in β-fraction for the compositions, exhibiting a modest increase near the end of solidification. As the Si content increases, we observe only a slight increase in the β-fraction. Thus, while Si has some influence on Fe-intermetallic formation, its effect is minor compared to that of Mn and Fe.

As already stated, A1 is a primary alloy, meaning that it has fewer tramp elements, as indicated in Table 3.3; how does it compare to A4, an alloy high in Fe and low in Mn? Figure 4.4 shows the experimental results from A4, which reveals a significant difference in the microstructure and morphology of the intermetallics compared to those in A1 (Figure 4.3). The figure displays numerous small intermetallics, a mixture of both α- and β-phases, with the majority falling within the 1-15 μm range. This could indicate that the β-phase starts to nucleate earlier in the solidification sequence, meaning that nucleation occurs at more nucleation sites; we also observe the β-phase appearing more frequently between the dendrites. Due to the increased content of Fe, the formation of α-phase intermetallics may occur alongside or even after the β-phase has started to form. There also appears to be a difference in the α-matrix and the Si eutectic region, where Si seems to be more abundant, which coincides with the higher Si content indicated in Table 3.3.

Spectrum 27 shows the typical composition of the aluminium matrix, which consists almost entirely of pure aluminium, reflecting the low solubility. In spectrum 28, we can also observe the typical composition of the Si eutectic region, characterised by a high Si content. Both of these phases comprise the majority of the volume fractions of the specimens, where we observed no other elements (with minor deviations) in these phases. As a result, the low solubility of other elements in aluminium leads to a conundrum when it comes to the content of intermetallic phases; it is almost impossible (or rather very expensive) to remove tramp elements entirely. Thus, showing the importance of properly controlling the relationship (primarily) between Fe and Mn.

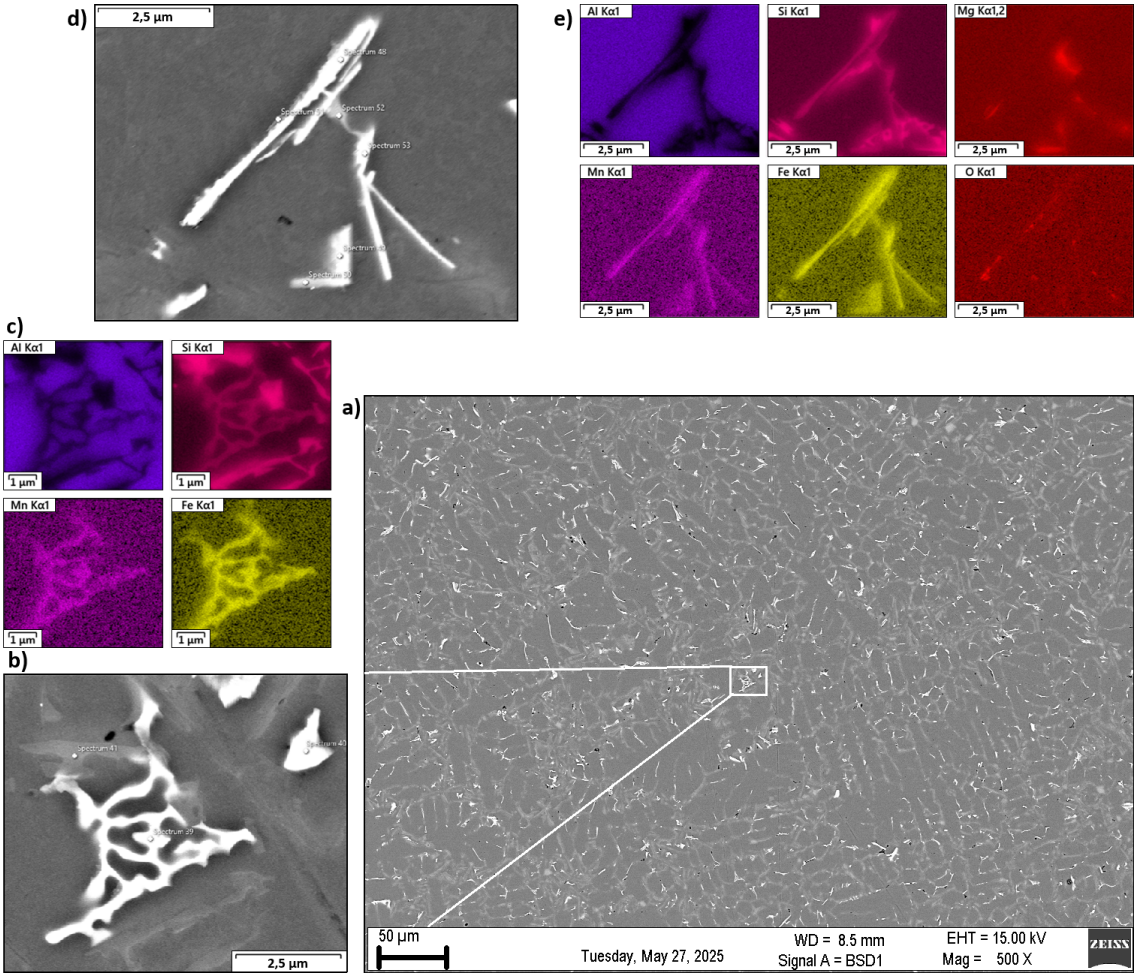

Figure 4.4: SEM-EDS mapping of sample A4, showing α, β and π Intermetallics: (a) SEM image of the microstructure, (b) Point map of α-phase, (c) EDS mapping of Al, Si, Mn and Fe for α-phase, (d) Point map of β- and π-phase, (e) EDS mapping of Al, Si, Mn, Fe, Mg and O for β- and π-phase.

To get a more quantitative comparison, the compositions of the intermetallics were measured using EDS point analysis and summarised in Table 4.3. The results coincide with relative comparison using EDS mapping. Spectrum 26 is from the suspected α-phase, as shown in Figure 4.3, and spectrum 39 in Figure 4.4. Here, we can observe a clear shift between Fe and Mn for the various compositions.

During the analysis, two different types of β-like phases were identified based on their morphology, with the smaller ones suspected to be the δ-phase. At the same time, their composition coincided very well with that of the β-phase, which has a lower Si content, as can be observed in spectra 31, 33, and 48. In contrast, the larger β-phase showed similarities to the δ compositions. Almost all phases vary from the theoretical stoichiometry, as presented in Table 3.4. To properly evaluate the phases and obtain a complete quantitative analysis, the inspection of the phases using the Kikuchi pattern with EBSD should be applied. However, this lies outside the scope

of this thesis. As discussed in the theory section, β and δ phases are very similar in appearance and can easily be mischaracterised.

Table 4.3: EDS composition results from A1 and A4

Label	Likely phase	Al	Si	Mn	Fe	Mg
A1 - Point measurement						
Spectrum 26	α	58.74	11.98	22.85	5.29	0.00
Spectrum 27	α-Al	97.03	1.08	0.29	0.00	0.00
Spectrum 28	Si eutectic	81.40	17.82	0.06	0.00	0.16
Spectrum 31	β or δ	76.98	13.35	6.63	2.32	0.16
Spectrum 33	β	52.90	25.12	16.95	4.34	0.07
Spectrum 34	β or δ	76.17	11.31	7.88	3.27	0.25
A4 - Point measurement						
Spectrum 39	α	56.81	21.12	4.34	15.41	0.61
Spectrum 48	β or δ	56.80	23.59	4.08	13.22	0.33
Spectrum 52	π	60.85	20.48	1.74	4.74	9.09

Notably, in Figure 4.4, there are slight traces of some oxide in the intermetallic, indicating impurities not accounted for in the simulations. More importantly, though, is the identified π-phase, which appears as a "smudge" attached to the β-phase. We can also identify it by its slightly brighter colour in the image with higher magnification (the point map in Figure 4.4 (d)), although it can easily be mistaken for Si-eutectic. As observed from both simulations and theory, the π-phase begins to form almost entirely after all liquid has solidified, utilising nucleation points such as the interfaces of the β intermetallics to form. It is important to note that the appearance of Mg_2Si could not be verified and validated.

4.3 The influence of magnesium

The role of magnesium in Al–Si–Fe–Mn alloys is twofold: it influences the as-cast microstructure via the formation of Mg-containing intermetallics, and it enables age hardening through Mg_2Si precipitation. Figure 4.5 and Table 4.4 illustrate how increasing Mg content (0.1–1.0 wt.%) affects the solidification path and final phase composition.

Figure 4.5 and Table 4.4 display the influence of increasing Mg content on the solidification behaviour and the intermetallic phase formation. While an increase in Mg up to 1 wt.% does not significantly affect the order of solidification (sequence of phase formation), it noticeably affects the solidification path, particularly in the final stages. A higher Mg content causes the onset temperature of α to increase while also shifting the onset of β formation and the entire eutectic region to solidify at a lower temperature, which correlates with the decrease in the onset of solidification for the system.

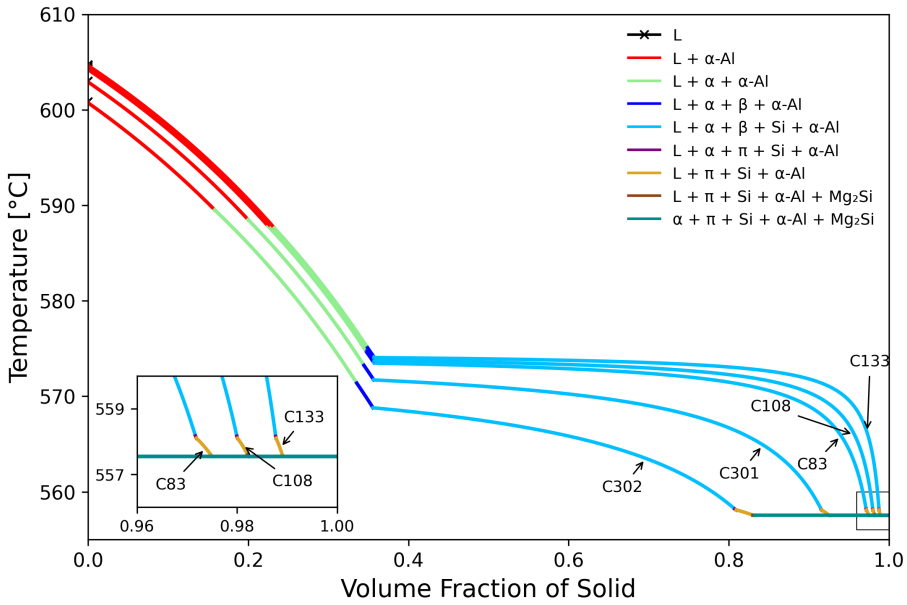

Figure 4.5: Scheil solidification curve for C83, C108, C133, C301 and C302 increasing Mg with a Fe/Mn ratio of 2.

Increased Mg content shifts the final eutectic region, where π-phase and Mg_2Si form. For higher content of Mg, it promotes the formation of the π-phase, which to some extent replaces the brittle β-Al_5FeSi phase in conjunction with Mn; this leads to a more compact, benign Chinese-script morphology in Fe-rich intermetallics. A higher Mg content also promotes the formation of Mg-based intermetallics, making the system more sensitive to variations in Mg content, such as evaporation of Mg during casting. Unexpected Mg evaporation can reduce Mg content, inadvertently increasing β-phase formation and leading to a decline in the expected material properties. As Mg content increases, the system increasingly favours π-phase formation, leading to Fe atoms being preferentially incorporated into the π-phase instead of forming β-phase intermetallics.

This behaviour is particularly evident in alloys C301 and C302, which contain the highest Mg levels. It has a significant effect on the solidification path in the final eutectic region ($L \rightarrow \alpha + \beta + Si + \alpha$-Al), which results in a more gradual slope for the solidification path than an abrupt transition. With more time to solidify, this may lead to more evenly distributed intermetallics, which in turn may influence both microsegregation patterns and the final microstructure morphology. As Mg increases, more Mg becomes available to precipitate as Mg_2Si, particularly in the eutectic region.

Notably, alloys with higher Mg levels (e.g., C302) exhibit significantly higher Mg_2Si fractions, while lower Mg alloys (e.g., C133) show almost no Mg_2Si, which indicates that most Mg remains in the solid solution. Thus, increased Mg content may enhance the potential for precipitation hardening by increasing the as-cast Mg-based

intermetallic content and the supersaturated solid solution within the α-Al matrix.

Table 4.4: Intermetallic phase fractions and compositions with increasing Mg.

Alloy	Onset Temperature (°C)		Volume Fraction [%]				
	α-Onset	β-Onset	α	β	FIMC	π	Mg_2Si
C133	587.6	575.1	0.86	1.27	2.14	0.02	0.00
C108	587.7	574.8	0.87	1.26	2.12	0.09	0.10
C83	587.8	574.6	0.87	1.25	2.12	0.12	0.15
C301	588.5	573.2	0.85	1.17	2.04	0.37	0.44
C302	589.5	571.4	0.88	1.01	1.89	0.85	1.00
Constant values: Si = 8.5 wt%, Fe = 0.6 wt%, Mn = 0.3 wt%							

4.4 Scheil simulations of evaporation

To evaluate the effect of uncontrolled process parameters, specifically the evaporation of Al and Mg, Figures 4.6 and 4.7 illustrate how these changes influence the solidification behaviour. The evaporation scenario simulated corresponds to a 10% loss of aluminium, which results in a relative increase in Si content (from 8.5 to 9.5 wt%) and a 20% loss of Mg (from 0.20 to 0.16%). Appendix Table A.10 provides the exact alloy compositions before and after evaporation.

The reduction of Mg content, although numerically small (0.04 wt%), significantly alters the solidification path. As shown in Table 4.5, the volume fraction of Mg_2Si decreased approximately from ∼0.12% to 0.10%. We also observe a reduction in the π-phase from approximately ∼0.15% to 0.11%, as the decreased availability of Mg favours the formation of FIMC instead. The unpredictability may negatively impact the potential of precipitation strengthening and degrade mechanical properties such as ductility.

The most predominant impact of evaporation stems from the increase in Si content, which alters the solidification sequence significantly. A higher Si content leads to a narrower solidification range for α-Al, which is consistent with established behaviour in Al-Si alloys. However, the combined effects of Al and Mg evaporation produce composition-dependent outcomes, leading to variability for both the solidification path and the resulting microstructure.

For the alloy pair shown in Figure 4.6 (a) (C303 and C308), we observe a delayed onset of the α-phase and an increased onset temperature for the β-phase, although its formation occurs later in the solidification path. In Figure 4.7, we observe an opposite trend for β-phase formation, as the onset temperature decreases, occurring earlier in the solidification process, whereas in Figure 4.6 (b), there are minimal changes to the onset temperatures and FIMC formations.

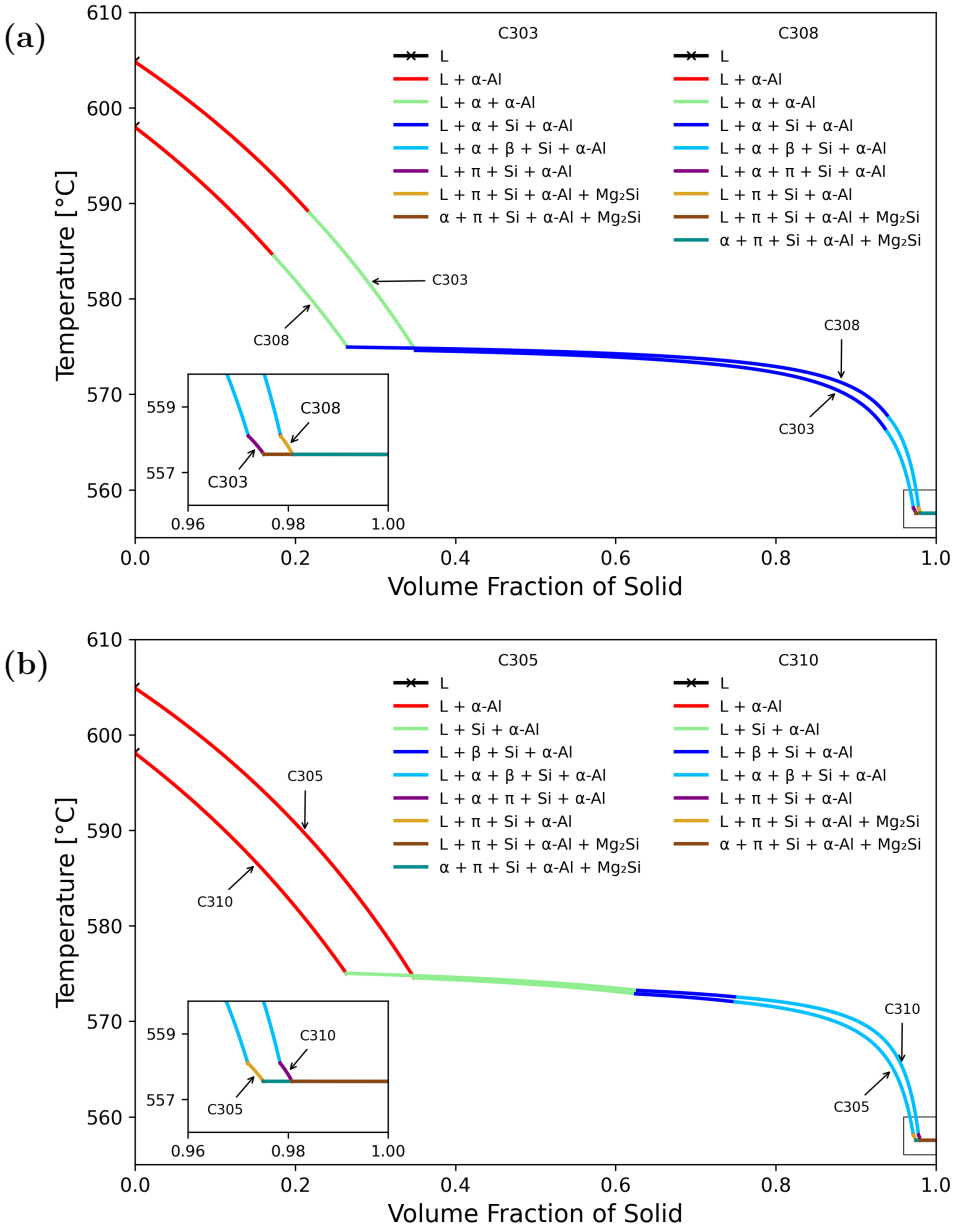

Figure 4.6: Scheil solidification curves simulating Al and Mg evaporation effects: (a) Compositions C303 and C308 with a Fe/Mn ratio of 0.2, (b) Compositions C305 and C310 with a Fe/Mn ratio of 3.0.

Some insight into the effects of evaporation is that there are unpredictable delays in α nucleation and unpredictable shifts in β onset temperatures, indicating a more complex interaction between the solute content and the phase stability. There are some key takeaways from the solidification path observations: the endpoint inset shows a decrease and shift in the eutectic plateau when all the liquid has solidified ($\alpha + \pi + \mathrm{Si} + \alpha\text{-Al} + \mathrm{Mg_2Si}$) due to the decrease in Mg. The overarching solidification sequence remains the same ($\mathrm{L} \rightarrow L + \alpha\text{-Al} \rightarrow L + \alpha\text{-Al} + \alpha \rightarrow ...$), but the exact proportions between the phases vary; in general, FIMC phase fractions increase and

Mg-based phases decrease with decreasing Mg.

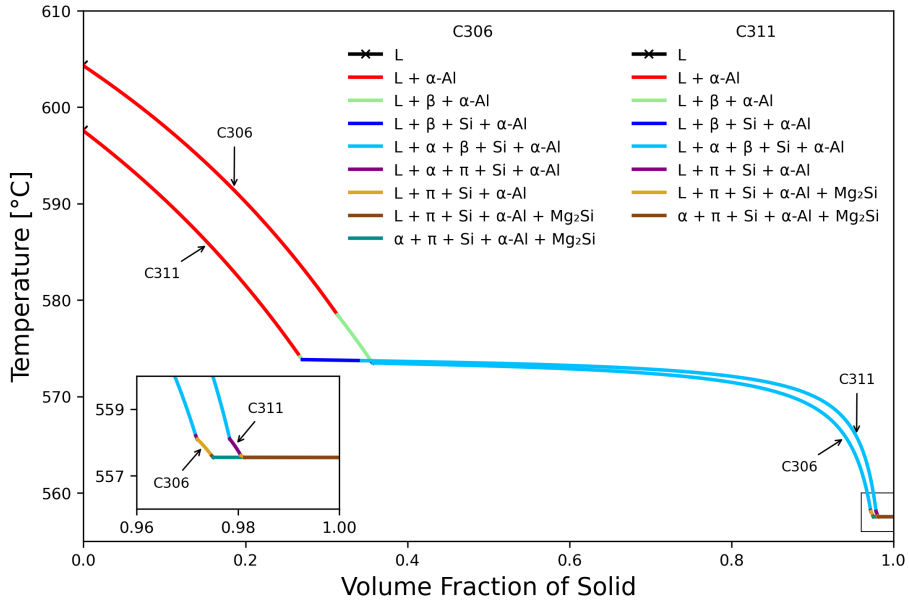

Figure 4.7: Scheil solidification curve for simulating the evaporation of Al and Mg for compositions C306 and C311 characterised by a higher Fe and Mn contents and a Fe/Mn ratio of 3.0.

These changes can have a significant impact from a materials engineer's point of view, especially in HPDC processes where control over solidification and variable microstructure is a common occurrence. The simulations help illustrate how solidification behaviour shifts, underlining the importance of minimising the effect of elemental evaporation. These changes may not be evident upon initial visual inspection; for example, a rise in Si-eutectic content may occur alongside a drop in Mg, which can be challenging to detect. The deviation from the targeted microstructure may only become apparent at a later stage, which shows the importance of maintaining control over process parameters.

Table 4.5: Comparison of phase fractions before and after evaporation.

Alloy	**Onset Temperature (°C)**		**Volume Fraction [%]**				
	α-Onset	**β-Onset**	α	β	FIMC	π	Mg_2Si
C303	589.0	566.1	1.05	0.06	1.12	0.15	0.12
C308	584.5	567.5	1.07	0.07	1.14	0.11	0.09
C305	572.0	572.9	0.17	0.75	0.92	0.15	0.12
C310	572.5	573.2	0.18	0.75	0.93	0.11	0.10
C306	573.5	578.5	0.46	1.48	1.94	0.15	0.12
C311	573.8	574.1	0.47	1.48	1.95	0.11	0.10
Si: 8.0 → 9.5 wt%, Mg: 0.20 → 0.16 wt%							

4.5 System data analysis

The beta phase

In Figure 4.8 (a), we can see the total fraction of β as a function of the Fe content, with Mn content presented by a colour scheme ranging from 0.1 to 1.2 wt.% shown to the left of the figure. A clear pattern emerges where the fraction of β-phase increases linearly with increased Fe content. The colour coding indicates that Mn readily suppresses the formation of β-phases, resulting in a decrease in the total amount of β-fraction.

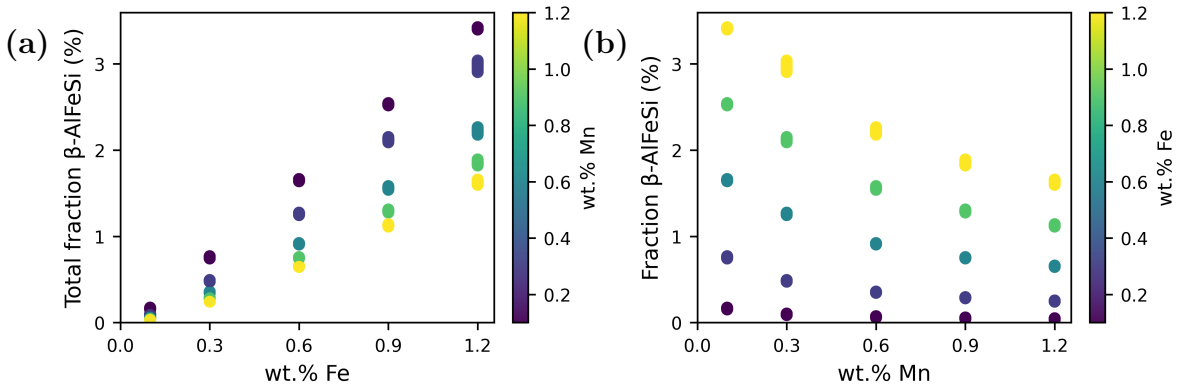

Figure 4.8: Relationship for total β fraction: (a) Between β-phase and Fe content, (b) β-phase and Mn content

It also appears that for a low Fe content of 0.10%, Mn will almost eliminate the formation of β, showing similar results to those of Erik Granhed et al. [35], with the exception that the β-phase is not suppressed entirely at higher Mn levels of >0.80%. This discrepancy may be due to the difference in cooling rate, specifically 100 K/s compared to 20 K/s in their work; even a Fe/Mn ratio of 0.08 does not eliminate the β-phase at high cooling rates in contrast to the result from Granhed.

In Figure 4.8 (b), we can see the relationship between the total fraction of β as a function of the Mn, represented using a colour gradient. The figure shows a more complicated non-linear hyperbolic trend: as Mn increases, the reduction in β-phase fraction becomes progressively smaller. This diminishing return indicates that while Mn has a suppressive effect on the β-phase at lower Fe concentrations, its influence weakens with further additions, particularly at higher Fe contents.

Increasing Mn content from 0.10 wt.% Mn to 0.30 wt.% results in a reduction of approximately 40% in β-fraction. A further increase to 0.60 wt.% Mn yields a 60% reduction, while at 1.20 wt.%, the β phase fraction is reduced by approximately 75%, relative to the baseline of 0.10 wt.% Mn. The corresponding values are summarised in Table 4.6, which highlights the strong suppressive effect of Mn on β-phase formation.

Table 4.6: Comparison of β-phase fraction at increasing Mn levels for different Fe contents.

Mn (wt.%)	**Mean β Fraction (%)**	**Decrease from Mn = 0.10 (%)**	**Observed β Range (%)**
Fe = 0.10 wt.%			
0.10	0.163	—	0.152 – 0.174
0.30	0.096	41.1%	0.087 – 0.105
0.60	0.066	59.7%	0.057 – 0.074
0.90	0.051	68.8%	0.042 – 0.059
1.20	0.042	74.5%	0.032 – 0.050
Fe = 0.30 wt.%			
0.10	0.757	—	0.742 – 0.770
0.30	0.484	36.1%	0.473 – 0.494
0.60	0.352	53.5%	0.344 – 0.360
0.90	0.288	61.9%	0.281 – 0.295
1.20	0.250	67.0%	0.242 – 0.256
Fe = 0.60 wt.%			
0.10	1.651	—	1.638 – 1.665
0.30	1.261	23.7%	1.245 – 1.275
0.60	0.914	44.7%	0.905 – 0.922
0.90	0.752	54.5%	0.743 – 0.760
1.20	0.653	60.4%	0.644 – 0.662
For the ranges: Si: 8.5 $\rightarrow$ 9.5 wt%, Mg: 0.10 $\rightarrow$ 0.20 wt%			

In comparison to Fe content of 0.3 and 0.6, we can see that the decrease in β-fraction in absolute percentage decreases at higher Mn content with a decreased slope after 0.6 wt.% Mn or when Fe/Mn = 1, as previously observed in Figure 4.8. This prompts the question: At what Mn concentration does further addition remain beneficial for suppressing the β-phase? We can thus draw the conclusion that the optimal range of Mn can thus be indicated to lie within 0.3 - 0.9 %, where the final compositional choice depends on the Fe content.

For optimising the material properties, the answer would be simple: we want no or as little Fe content as possible. However, for increased recycled content, there is an inherent increase in impurities. As Raabe et al. [3] advocate for higher tolerances to tramp elements and composition variation, we can draw some general conclusions. We should strive for a Fe/Mn ratio of 0.5, taking into account slight variations in composition while also considering the solidification path and other composition guidelines, such as the sludge factor.

Based on the CALPHAD calculations from Erik Granhed et al. [35], the sludge factor should not exceed $\sim$1.3 to avoid sludge formation. However, this may not conflict with the SF for higher Fe content. Higher Fe content also makes the system

more sensitive to composition variation, which contradicts the aim of making the alloy more tolerant to such fluctuations.

The alpha phase

In contrast to the β-phase, there is no linear relationship between α-fraction and the Fe content. In Figure 4.9 (a), we can see the composition-phase fraction relationship for α as a function of Fe, where Mn content is presented using a colour scheme. It demonstrates the α-fraction increases with both Fe and Mn at levels above 0.1 wt.%.

At lower levels (0.1 wt.% Mn), the α fraction even decreases as the β-phase becomes dominant. At levels of Mn, up to 0.3 wt.%, the increase in Fe is roughly linear for the formation of the α-phase, after which it is a monotonically increasing concave curvature (meaning it curves inward in contrast to Figure 4.8 (b)) with a compositional dependency as shown in Figure 4.9 (a). This indicates that at higher Fe content, the suppressive effect of Mn becomes limited.

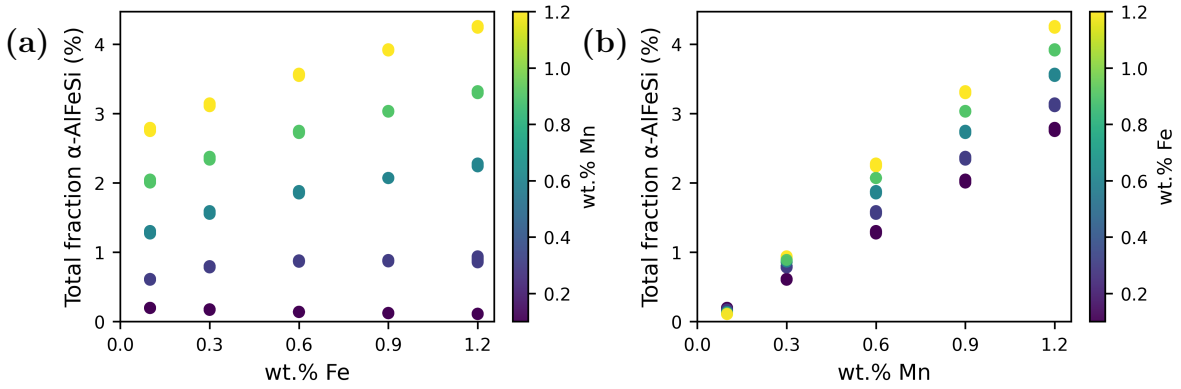

Figure 4.9: Relationship for total α fraction: (a) Between α-phase and Fe content, (b) α-phase and Mn content

For the relationship between the α-phase and Mn, a strong linear relationship is observed, as presented in Figure 4.9 (b), which illustrates the effect of Mn on α-phase formation, where Fe is indicated using a colour scheme. Here, the relationship is the opposite of that of β and Fe in Figure 4.8, with a steeper slope and smaller span with higher content of Fe.

As shown in Figure 4.8, the slope of β-fraction decreases uniformly with increased Fe content. However, a change occurs between 0.3 wt.% and 0.6 wt.% Mn. This trend is consistent across most Fe levels, with the exception of the 0.1–0.3 wt.% Fe range, as also observed in Table 4.6. Essentially, we can observe the same relationship from a different perspective; this is also reflected in the total content of FIMC.

Total FIMC

To fully understand FIMC formation, it is important to note that at higher Mg levels, the π-phase also contributes. In this work, we intentionally kept the Mg content low to influence the solidification path primarily. Figure 4.10 shows the total

volume fraction of FIMC compared to Fe content. It presents the total fraction of β fractions from 4.8 added together with total α fractions from 4.9, showing the increase in intermetallic fractions based on the Fe and Mn content for their respective compositions.

We can see that the relationship is strongly linear, with the same slope for all Fe/Mn ratios, which concurs with the literature, as Mn and Fe can be substituted interchangeably in the α- and β-phases. An important, though seemingly obvious, insight is that increasing both Fe and Mn always raises the total fraction of FIMC; however, we can alter the ratio between α- and β-phases by adjusting their relative concentrations. In comparison to the two plots in Figure 4.10, we can see that the volume fraction increase of FIMC has a broader span with increased Fe content.

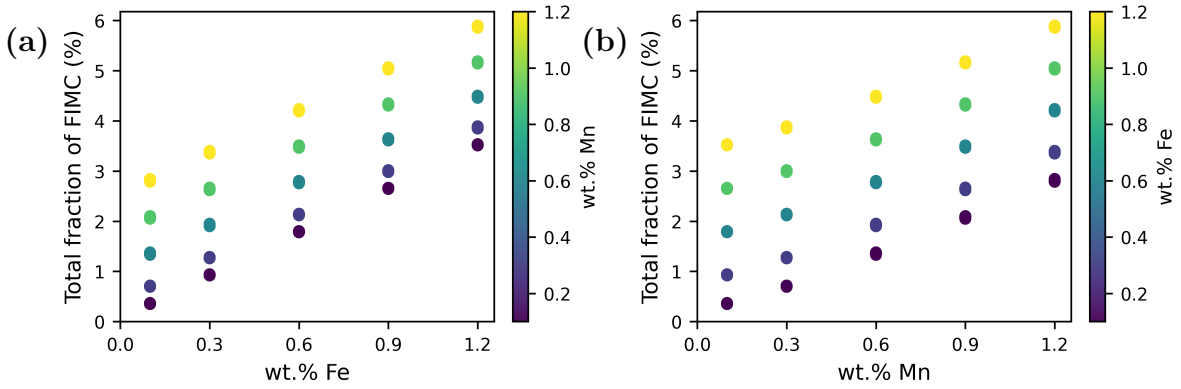

Figure 4.10: Relationship for total FIMC volume fraction: (a) Between FIMC and Fe content, (b) FIMC and Mn content.

4.6 Observed kinetic effects

The Scheil simulations do not fully capture some key factors. In addition to the suspected formation of the δ phase, other key kinetic phenomena have been observed in the SEM when conducting the experimental analysis.

One such observation can be seen in Figure 4.11 (where A6 exhibits a similar composition to A1 as shown in Table 3.3). It shows indications of a similar microstructure as A1 with larger clusters of α intermetallics and small intermetallics clutching the dendrites of the α-Al matrix. A distinct microstructural deviation appears in the upper/centre-right corner, where an area with large β-phase particles has accumulated.

As discussed, heavier elements such as intermetallics exhibit a brighter contrast from BSE, aside from the prominent needle-like β- and the more compact α-phases structures; we only see the darker α-Al matrix and the Si-eutectic region. The large cluster with β-phase particles could be due to local differences in the cooling rate where the β-phase grows if there is a lower cooling rate at that specific area. Another

explanation could be a local Mg depletion due to uneven distribution or evaporation. This could be due to Fe not being drawn to the π-phase, thus leading to more β-phase formation. This is plausible, as there appear to be no small intermetallics that typically form and adhere to the α-Al matrix. This is in contrast to the upper left corner of Figure 4.11, where there appears to be a local increase in the formation of these small intermetallics. This should be further studied and measured using EDS mapping of the area before a conclusion is drawn as the absolute cause.

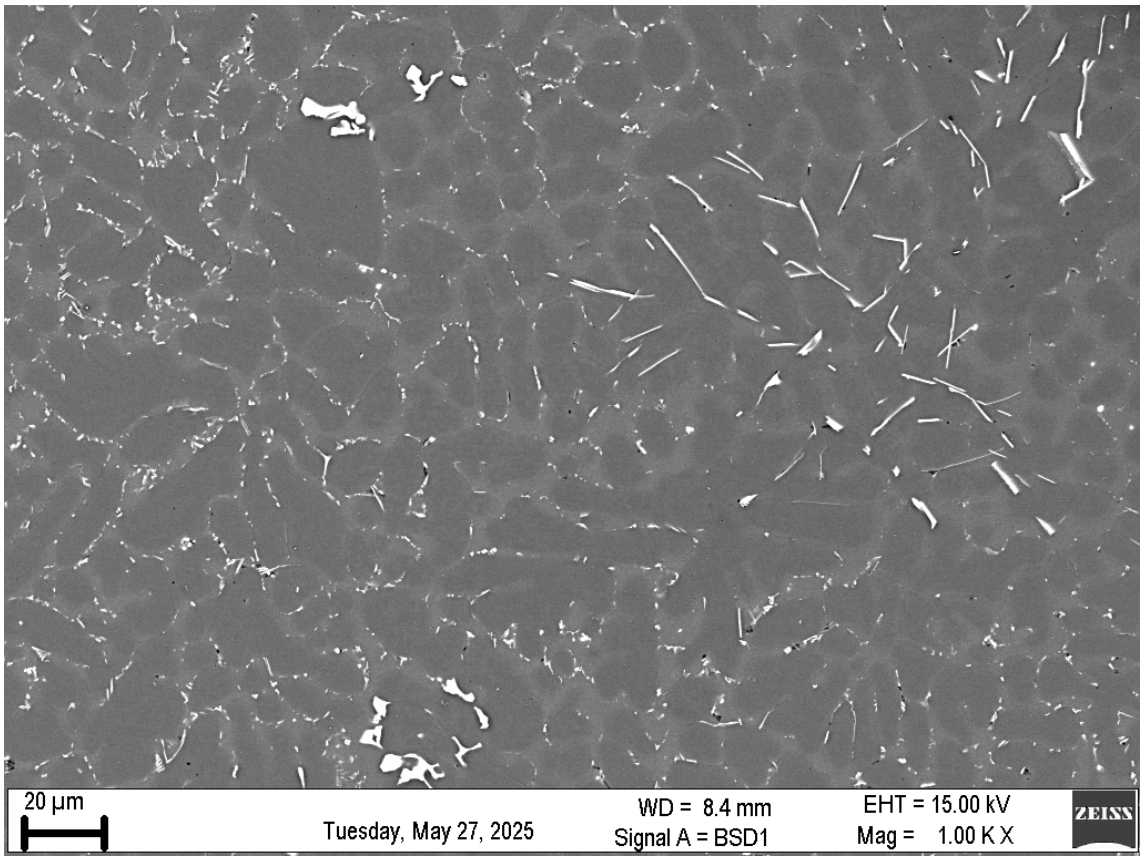

Figure 4.11: SEM of the microstructure for A6, showing uneven phase distributions, indicating segregation due to local cooling rate deviations.

In Figure 4.12, a similar effect is observed, where the α phase has been enriched and gathered heavier elements, Fe and Mn, from the surrounding melt. This is the effect of the α-phase forming early on in the solidification path, where it locally depletes these elements near the growing intermetallic. This results in a local solute depletion zone for these elements. The effect can also be seen to a lesser extent in Figure 4.3 around the large α-phases. Under rapid cooling rates, such as in this case, limited diffusion prevents further re-homogenisation, which inhibits the formation of other FIMCs in the vicinity. This phenomenon exemplifies how local intermetallic phases compete for solute during non-equilibrium solidification, where limited time prevents improper elemental diffusion.

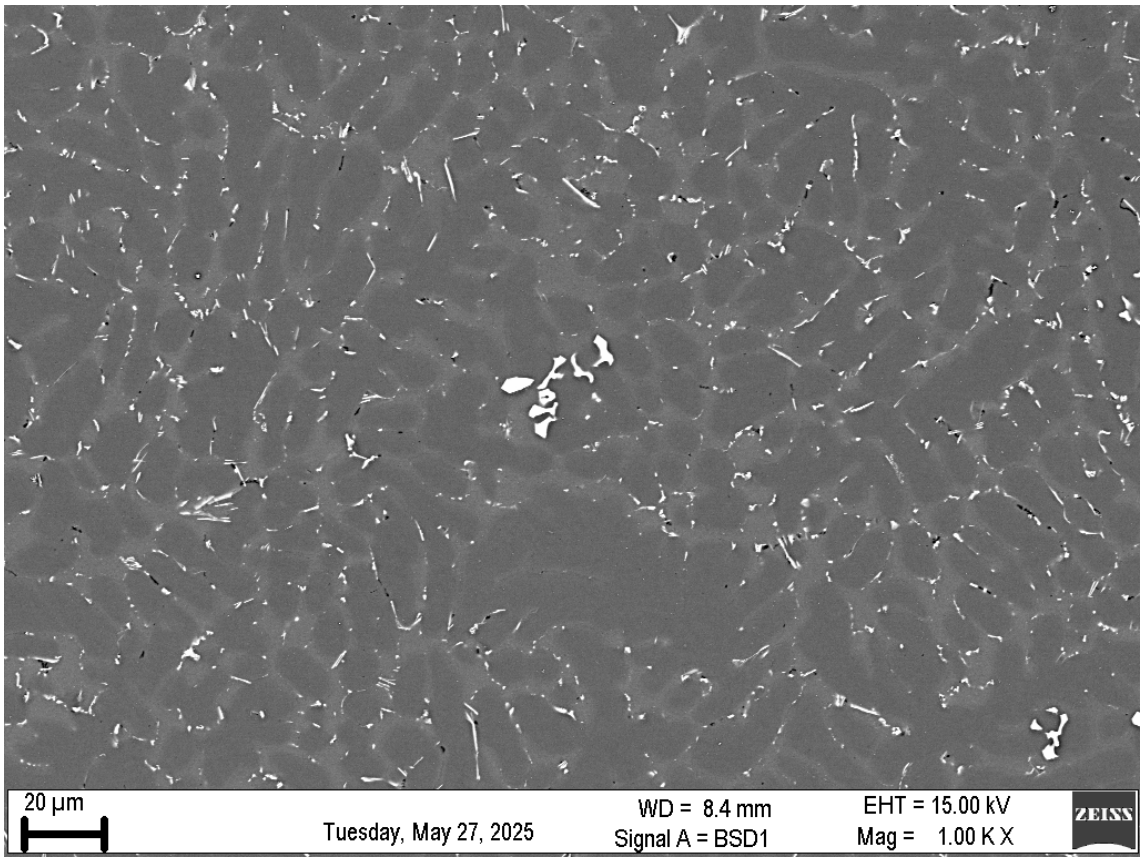

Figure 4.12: SEM image showing solute depletion around alpha intermetallic.

5
Conclusion

The findings in this thesis show that the formation of the β-Al_5FeSi and the more benign α-$Al_{15}(Fe,Mn)_3Si_2$ phases are susceptible to the Fe/Mn ratio and the local availability of Mg and Si. Using a defined grid of parametric simulations in conjunction with analysis of the microstructure by SEM, it is observed that a shift in Mn content favours the phase formation of the α, thus suppressing the formation of the β-phase. Similarly, higher Fe content promotes earlier β-phase nucleation, especially when Mn is low. This dynamic is influenced further by Si content, which alters the solidification path and their onset temperatures. Additionally, the presence of Mg causes the formation of the π-phase to occur, which influences the eutectic phase formation during the final stages of solidification, where elevated content of Mg may prioritise the formation of the π-phase. As a result, there is a decrease in the β-fraction. This may make the material's mechanical properties more sensitive to casting side effects such as evaporation.

To enhance the predictive realism of CALPHAD simulations, SDAS measurements were integrated for the Scheil-Gulliver solidification model while also applying approximate kinetic undercooling through back-diffusion effects in the model. This bridges the gap between equilibrium-based phase predictions and microstructure analysis. The simulated solidification paths predict the onset, sequence and pattern of the multiphase eutectic reactions. The results explain the composition dependency of the solidification domains for the π-, α-, β-, and Mg_2Si phases, where complementary microstructure analysis demonstrates the suppression of the β-Al_5FeSi phase in Mn-rich alloys and the increased appearance of the π phase with increasing Mg content. The framework validates the thermodynamic predictions with physical features from SEM micrographs and predicts intermetallic formations. While Scheil solidification simulations do not explicitly provide microstructural morphology, we can infer trends based on phase fractions, compositions and the order of the phase formation. An example is the α-phase forming before the Si-eutectic, while the β-phase in later stages may lead to larger α-intermetallics. Thus, depleting the local solute of other heavy elements, such as Fe and Mn, effectively reduces the size of other intermetallics.

The system data analysis shows visible correlations between alloy compositions, solidification behaviour and the formation of intermetallic phases. There was a linear correlation with increased Fe content on β-phase formation, where Mn content continuously shifted the phase stability toward the formation of α-phase. Thus reducing the volume fraction of β and delaying its onset temperature. This trend

becomes more pronounced with higher Fe/Mn ratios to a Fe/Mn ratio of 1 or a Mn content of ∼0.6 wt.%, where Mn becomes more readily available to substitute Fe in the phase formation of intermetallics. At higher Mn content or lower Fe/Mn ratio, the effect persists but is less profound, raising the question of a cost-benefit analysis. Both phase fraction plots and experimental SEM images verified the trend.

Future work could comprise encompassing these findings by incorporating kinetic simulations such as DICTRA, applying more advanced crystallographic verification methods such as EBSD, verification of phase fraction from experimental samples, investigation of the sensitivity of the system to variable cooling rates, the integration of machine learning-driven alloy design and its correlation with the mechanical properties to get a holistic view between composition, process, and performance.

Bibliography

[1] International Aluminium Institute. *Greenhouse Gas Emissions Decline in Aluminium Industry*. 2024. URL: https://international-aluminium.org/resource/greenhouse-gas-emissions-decline-in-aluminium-industry/.

[2] International Aluminium Institute. *IAI Material Flow Move – 2021 update*. 2021. URL: https://international-aluminium.org/resource/iai-material-flow-model-2021-update/.

[3] Dierk Raabe et al. "Making Sustainable Aluminum by Recycling Scrap: The Science of "Dirty" Alloys". In: *Progress in Materials Science* 128 (2022). DOI: 10.1016/j.pmatsci.2022.100947.

[4] A. Casadei and R. Broda. "Impact of vehicle weight reduction on fuel economy for various vehicle architectures". In: (2024). URL: https://vanconverts.com/wp-content/uploads/Ricardo_FE_MPG_Study-1.pdf.

[5] International Aluminium Institute. *Historical Statistics*. 2023. URL: https://www.international-aluminium.org/statistics/primary-aluminium-smelting-power-consumption/.

[6] R. Kakitani et al. "The roles of solidification cooling rate and (Mn,Cr) alloying elements in the modification of -AlFeSi and hardness evolvements in near-eutectic Al-Si alloys". In: *Journal of Alloys and Metallurgical Systems* 1 (2023), p. 100005. ISSN: 2949-9178. DOI: 10.1016/j.jalmes.2023.100005.

[7] M. Tiryakioğlu. "Intrinsic and Extrinsic Effects of Microstructure on Properties in Cast Al Alloys". In: *Materials* 13 (9 2020), p. 2019. DOI: 10.3390/ma13092019.

[8] L. Ceschini et al. "Correlation between ultimate tensile strength and solidification microstructure for the sand cast A357 aluminium alloy". In: *Materials & Design* 30 (10 2009), pp. 4525–4531. DOI: 10.1016/j.matdes.2009.05.012.

[9] R. S. Gendron, M. Ingulstad, and E. Storli. *Aluminum Ore: The Political Economy of the Global Bauxite Industry*. University of British Columbia Press, 2013.

[10] U.S. Geological Survey. *Mineral Commodity Summaries 2023*. 2023. DOI: 10.3133/mcs2023.

[11] John Campbell. *Complete Casting Handbook: Metal Casting Processes, Metallurgy, Techniques and Design*. Elsevier Science & Technology, 2015. ISBN: 9780081001227.

[12] ASM International Handbook Committee. *ASM Handbook, Volume 15 - Casting*. ASM International, 2008; 2010. ISBN: 978-0-87170-711-6.

[13] Bin Sun et al. “Study on Al Evaporation during AlV55 Melting and Alloy Preparation”. In: *Metals* 14.4 (2024). ISSN: 2075-4701. DOI: 10.3390/met14040466.

[14] Inductiveload. *Cold chamber die casting schematic*. https://commons.wikimedia.org/wiki/File:Cold_chamber.png. Public domain via Wikimedia Commons. 2008.

[15] Ian Polmear et al. *Light Alloys: Metallurgy of the Light Metals*. United States of America: Academic Press, 2017. ISBN: 9780080994314.

[16] J.G. Kaufman, E.L. Rooy, and American Foundry Society. *Aluminum Alloy Castings: Properties, Processes, and Applications*. ASM International, 2004. ISBN: 9780871708038.

[17] J. R. Davis and J. Davis. *Alloying: Understanding the Basics*. ASM International, 2001.

[18] Kevin Weritz, John Kaufman, and J. Gilbert Anderson. *ASM Handbook®, Volume 02B - Properties and Selection of Aluminum Alloys*. ASM International, 2019. DOI: 10.31399/asm.hb.v02b.9781627082105.

[19] Dominik Bösch et al. “Secondary Al-Si-Mg High-pressure Die Casting Alloys with Enhanced Ductility”. In: *Metallurgical and Materials Transactions A* 46 (2014), pp. 1–11. DOI: 10.1007/s11661-014-2700-8.

[20] Zhongping Que et al. “Understanding Fe-Containing Intermetallic Compounds in Al Alloys: An Overview of Recent Advances from the LiME Research Hub”. In: *Metals* 12.10 (2022). ISSN: 2075-4701. DOI: 10.3390/met12101677.

[21] Waleed Mohammed et al. “Thermodynamics-guided design of sustainable secondary Al-Si alloys for enhanced Fe-impurity tolerance and optimized Mn doping”. In: *Acta Materialia* 289 (2025), p. 120932. ISSN: 1359-6454. DOI: 10.1016/j.actamat.2025.120932.

[22] E. Samuel et al. “Intermetallic phases in Al–Si based cast alloys: new perspective”. In: *International Journal of Cast Metals Research* 27 (2 2013), pp. 107–114. DOI: 10.1179/1743133613Y.0000000083.

[23] Williams Ebhota and Tien-Chien Jen. “Intermetallics Formation and Their Effect on Mechanical Properties of Al-Si-X Alloys”. In: (2018). DOI: 10.5772/intechopen.73188.

[24] Michael V. Glazoff et al. *Casting Aluminum Alloys: Their Physical and Mechanical Metallurgy*. 2nd. Elsevier, 2019. ISBN: 978-0-12-811805-4.

[25] H. Becker et al. “Effect of Mn and cooling rates on α-, β- and δ-Al–Fe–Si intermetallic phase formation in a secondary Al–Si alloy”. In: *Materialia* 5 (2019), p. 100198. ISSN: 2589-1529. DOI: 10.1016/j.mtla.2018.100198.

[26] Hai-lin Chen et al. “Update of Al-Fe-Si, Al-Mn-Si and Al-Fe-Mn-Si thermodynamic descriptions”. In: *Transactions of Nonferrous Metals Society of China* 24.7 (2014), pp. 2041–2053. ISSN: 1003-6326. DOI: 10.1016/S1003-6326(14)63310-0.

[27] John A. Taylor. “Iron-Containing Intermetallic Phases in Al-Si Based Casting Alloys”. In: *Procedia Materials Science* 1 (2012). 11th International Congress on Metallurgy & Materials SAM/CONAMET 2011, pp. 19–33. ISSN: 2211-8128. DOI: 10.1016/j.mspro.2012.06.004.

[28] Nikolay A. Belov, Dmitry G. Eskin, and Andrey A. Aksenov. *Multicomponent Phase Diagrams: Applications for Commercial Aluminum Alloys*. Elsevier, 2005. ISBN: 978-0-08-044537-3. DOI: 10.1016/B978-0-08-044537-3.X5000-8.

[29] Bruna Callegari, Tiago Nunes Lima, and Rodrigo Santiago Coelho. "The Influence of Alloying Elements on the Microstructure and Properties of Al-Si-Based Casting Alloys: A Review". In: *Metals* 13.7 (2023). ISSN: 2075-4701. DOI: 10.3390/met13071174.

[30] J. Gobrecht. "Gravity-Segregation of Iron, Manganese and Chromium in an Aluminum-Silicon Casting, Part I". In: *Giesserei* 61.10 (1975), pp. 263–265.

[31] J. L. Jarstad. "Understanding Sludge". In: *Proceedings of the 14th SDCE International Die Casting Congress and Exposition*. Paper No. G-T87-011. Toronto, Ontario, Canada, May 1987.

[32] S.G. Shabestari. "The effect of iron and manganese on the formation of intermetallic compounds in aluminum–silicon alloys". In: *Materials Science and Engineering: A* 383.2 (2004), pp. 289–298. ISSN: 0921-5093. DOI: 10.1016/j.msea.2004.06.022.

[33] S.G. Shabestari and J. Gruzleski. "Gravity segregation of complex intermetallic compounds in liquid aluminum-silicon alloys". In: *Metallurgical and Materials Transactions A* 26 (Apr. 1995), pp. 999–1006. DOI: 10.1007/BF02649097.

[34] Makhlouf M Makhlouf and Diran Apelian. *Casting Characteristics of Aluminum Die Casting Alloys*. Tech. rep. Worcester Polytechnic Institute (US), Feb. 2002. DOI: 10.2172/792701. URL: https://www.osti.gov/biblio/792701.

[35] Erik Granhed et al. "A CALPHAD-Based Investigation of the Sludge Factor". In: *International Journal of Metalcasting* 18 (Apr. 2024), pp. 343–351. DOI: 10.1007/s40962-023-01018-5.

[36] M. J. Castro-Román et al. "Role of Fe/Mn Ratio and Cooling Rate on Precipitation of Iron Intermetallics -AlFeMnSi and -AlFeSi in a 356 Alloy". In: *Transactions of the Indian Institute of Metals* 68 (2015), pp. 1193–1197. DOI: 10.1007/s12666-015-0703-9.

[37] X. Cao and J. Campbell. "The Nucleation of Fe-Rich Phases on Oxide Films in Al-11.5Si-0.4Mg Cast Alloys". In: *Metallurgical and Materials Transactions A* 34 (2003), pp. 1409–1420. DOI: 10.1007/s11661-003-0253-3.

[38] X. Cao and J. Campbell. "Effect of Sr on primary -Fe phase in liquid Al-11.5 Si-0.4 Mg cast alloy". In: *Materials Science and Technology* 20.4 (2004), pp. 514–520. DOI: 10.1179/026708304225019030.

[39] W. Kurz, D.J. Fisher, and M. Rappaz. *Fundamentals of Solidification 5th Edition*. Foundations of Materials Science and Engineering. Trans Tech Publications Limited, 2023. ISBN: 9783036410159.

[40] Ibrahim Sari et al. "Prediction of the Secondary Arms Spacing Based on Dendrite Tip Kinetics and Cooling Rate". In: *Materials* 17.4 (2024). ISSN: 1996-1944. DOI: 10.3390/ma17040865. URL: https://www.mdpi.com/1996-1944/17/4/865.

[41] John Campbell and Murat Tiryakioğlu. “Fatigue Failure in Engineered Components and How It Can Be Eliminated: Case Studies on the Influence of Bifilms”. In: *Metals* 12.8 (2022). ISSN: 2075-4701. DOI: 10.3390/met12081320.

[42] John Campbell. “An overview of the effects of bifilms on the structure and properties of cast alloys”. In: *Metallurgical and Materials Transactions B* 37 (Dec. 2006), pp. 857–863. DOI: 10.1007/BF02735006.

[43] M. C. Flemings. “Solidification Processing”. In: *Metallurgical Transactions* 5.10 (1974), pp. 2121–2134. ISSN: 2379-0083. DOI: 10.1007/BF02643923.

[44] Prince Anyalebechi. “Effects of alloying elements and solidification conditions on secondary dendrite arm spacing in aluminum alloys”. In: *TMS Annual Meeting* (Jan. 2004), pp. 217–233.

[45] J. B. Wiskel et al. “Solidification Study of Aluminum Alloys Using Impulse Atomization: Part II. Effect of Cooling Rate on Microstructure”. In: *Canadian Metallurgical Quarterly* 41.2 (2002), pp. 193–204. DOI: 10.1179/cmq.2002.41.2.193.

[46] Hai-lin CHEN et al. “Update of Al-Fe-Si, Al-Mn-Si and Al-Fe-Mn-Si thermodynamic descriptions”. In: *Transactions of Nonferrous Metals Society of China* 24 (7 2014), pp. 2041–2053. DOI: 10.1016/S1003-6326(14)63310-0.

[47] D.A. Porter, K.E. Easterling, and M.Y. Sherif. *Phase Transformations in Metals and Alloys*. 4th. CRC Press, 2021. DOI: 10.1201/9781003011804.

[48] Tatu Pinomaa, Anssi Laukkanen, and Nikolas Provatas. “Solute Trapping in Rapid Solidification”. In: *MRS Bulletin* 45.11 (2020), pp. 910–915. ISSN: 1938-1425. DOI: 10.1557/mrs.2020.274.

[49] Hydrargyrum. *Bragg Diffraction Diagram*. https://commons.wikimedia.org/wiki/File:Bragg_diffraction_2.svg. Own work, licensed under CC BY-SA 3.0. 2010. URL: https://commons.wikimedia.org/w/index.php?curid=17543875.

A

Compositions simulated

Table A.1: Compositions (C1 - C32) with varying Si, Fe, Mn, Mg (wt%).

Alloy	Si (wt%)	Fe (wt%)	Mn (wt%)	Mg (wt%)	Fe/Mn Ratio	SF
C1	8.0	0.10	0.10	0.20	1.00	0.30
C2	8.0	0.30	0.10	0.20	3.00	0.50
C3	8.0	0.60	0.10	0.20	6.00	0.80
C4	8.0	0.90	0.10	0.20	9.00	1.10
C5	8.0	1.20	0.10	0.20	12.00	1.40
C6	8.0	0.10	0.30	0.20	0.33	0.70
C7	8.0	0.30	0.30	0.20	1.00	0.90
C8	8.0	0.60	0.30	0.20	2.00	1.20
C9	8.0	0.90	0.30	0.20	3.00	1.50
C10	8.0	1.20	0.30	0.20	4.00	1.80
C11	8.0	0.10	0.60	0.20	0.17	1.30
C12	8.0	0.30	0.60	0.20	0.50	1.50
C13	8.0	0.60	0.60	0.20	1.00	1.80
C14	8.0	0.90	0.60	0.20	1.50	2.10
C15	8.0	1.20	0.60	0.20	2.00	2.40
C16	8.0	0.10	0.90	0.20	0.11	1.90
C17	8.0	0.30	0.90	0.20	0.33	2.10
C18	8.0	0.60	0.90	0.20	0.67	2.40
C19	8.0	0.90	0.90	0.20	1.00	2.70
C20	8.0	1.20	0.90	0.20	1.33	3.00
C21	8.0	0.10	1.20	0.20	0.08	2.50
C22	8.0	0.30	1.20	0.20	0.25	2.70
C23	8.0	0.60	1.20	0.20	0.50	3.00
C24	8.0	0.90	1.20	0.20	0.75	3.30
C25	8.0	1.20	1.20	0.20	1.00	3.60
C26	8.0	0.10	0.10	0.15	1.00	0.30
C27	8.0	0.30	0.10	0.15	3.00	0.50
C28	8.0	0.60	0.10	0.15	6.00	0.80
C29	8.0	0.90	0.10	0.15	9.00	1.10
C30	8.0	1.20	0.10	0.15	12.00	1.40
C31	8.0	0.10	0.30	0.15	0.33	0.70
C32	8.0	0.30	0.30	0.15	1.00	0.90

Table A.2: Compositions (C33 - C65) with varying Si, Fe, Mn, Mg (wt%).

Alloy	Si (wt%)	Fe (wt%)	Mn (wt%)	Mg (wt%)	Fe/Mn Ratio	SF
C33	8.0	0.60	0.30	0.15	2.00	1.20
C34	8.0	0.90	0.30	0.15	3.00	1.50
C35	8.0	1.20	0.30	0.15	4.00	1.80
C36	8.0	0.10	0.60	0.15	0.17	1.30
C37	8.0	0.30	0.60	0.15	0.50	1.50
C38	8.0	0.60	0.60	0.15	1.00	1.80
C39	8.0	0.90	0.60	0.15	1.50	2.10
C40	8.0	1.20	0.60	0.15	2.00	2.40
C41	8.0	0.10	0.90	0.15	0.11	1.90
C42	8.0	0.30	0.90	0.15	0.33	2.10
C43	8.0	0.60	0.90	0.15	0.67	2.40
C44	8.0	0.90	0.90	0.15	1.00	2.70
C45	8.0	1.20	0.90	0.15	1.33	3.00
C46	8.0	0.10	1.20	0.15	0.08	2.50
C47	8.0	0.30	1.20	0.15	0.25	2.70
C48	8.0	0.60	1.20	0.15	0.50	3.00
C49	8.0	0.90	1.20	0.15	0.75	3.30
C50	8.0	1.20	1.20	0.15	1.00	3.60
C51	8.0	0.10	0.10	0.10	1.00	0.30
C52	8.0	0.30	0.10	0.10	3.00	0.50
C53	8.0	0.60	0.10	0.10	6.00	0.80
C54	8.0	0.90	0.10	0.10	9.00	1.10
C55	8.0	1.20	0.10	0.10	12.00	1.40
C56	8.0	0.10	0.30	0.10	0.33	0.70
C57	8.0	0.30	0.30	0.10	1.00	0.90
C58	8.0	0.60	0.30	0.10	2.00	1.20
C59	8.0	0.90	0.30	0.10	3.00	1.50
C60	8.0	1.20	0.30	0.10	4.00	1.80
C61	8.0	0.10	0.60	0.10	0.17	1.30
C62	8.0	0.30	0.60	0.10	0.50	1.50
C63	8.0	0.60	0.60	0.10	1.00	1.80
C64	8.0	0.90	0.60	0.10	1.50	2.10
C65	8.0	1.20	0.60	0.10	2.00	2.40

Table A.3: Compositions (C66 - C98) with varying Si, Fe, Mn, Mg (wt%).

Alloy	Si (wt%)	Fe (wt%)	Mn (wt%)	Mg (wt%)	Fe/Mn Ratio	SF
C66	8.0	0.10	0.90	0.10	0.11	1.90
C67	8.0	0.30	0.90	0.10	0.33	2.10
C68	8.0	0.60	0.90	0.10	0.67	2.40
C69	8.0	0.90	0.90	0.10	1.00	2.70
C70	8.0	1.20	0.90	0.10	1.33	3.00
C71	8.0	0.10	1.20	0.10	0.08	2.50
C72	8.0	0.30	1.20	0.10	0.25	2.70
C73	8.0	0.60	1.20	0.10	0.50	3.00
C74	8.0	0.90	1.20	0.10	0.75	3.30
C75	8.0	1.20	1.20	0.10	1.00	3.60
C76	8.5	0.10	0.10	0.20	1.00	0.30
C77	8.5	0.30	0.10	0.20	3.00	0.50
C78	8.5	0.60	0.10	0.20	6.00	0.80
C79	8.5	0.90	0.10	0.20	9.00	1.10
C80	8.5	1.20	0.10	0.20	12.00	1.40
C81	8.5	0.10	0.30	0.20	0.33	0.70
C82	8.5	0.30	0.30	0.20	1.00	0.90
C83	8.5	0.60	0.30	0.20	2.00	1.20
C84	8.5	0.90	0.30	0.20	3.00	1.50
C85	8.5	1.20	0.30	0.20	4.00	1.80
C86	8.5	0.10	0.60	0.20	0.17	1.30
C87	8.5	0.30	0.60	0.20	0.50	1.50
C88	8.5	0.60	0.60	0.20	1.00	1.80
C89	8.5	0.90	0.60	0.20	1.50	2.10
C90	8.5	1.20	0.60	0.20	2.00	2.40
C91	8.5	0.10	0.90	0.20	0.11	1.90
C92	8.5	0.30	0.90	0.20	0.33	2.10
C93	8.5	0.60	0.90	0.20	0.67	2.40
C94	8.5	0.90	0.90	0.20	1.00	2.70
C95	8.5	1.20	0.90	0.20	1.33	3.00
C96	8.5	0.10	1.20	0.20	0.08	2.50
C97	8.5	0.30	1.20	0.20	0.25	2.70
C98	8.5	0.60	1.20	0.20	0.50	3.00

Table A.4: Compositions (C99 - C131) with varying Si, Fe, Mn, Mg (wt%).

Alloy	Si (wt%)	Fe (wt%)	Mn (wt%)	Mg (wt%)	Fe/Mn Ratio	SF
C99	8.5	0.90	1.20	0.20	0.75	3.30
C100	8.5	1.20	1.20	0.20	1.00	3.60
C101	8.5	0.10	0.10	0.15	1.00	0.30
C102	8.5	0.30	0.10	0.15	3.00	0.50
C103	8.5	0.60	0.10	0.15	6.00	0.80
C104	8.5	0.90	0.10	0.15	9.00	1.10
C105	8.5	1.20	0.10	0.15	12.00	1.40
C106	8.5	0.10	0.30	0.15	0.33	0.70
C107	8.5	0.30	0.30	0.15	1.00	0.90
C108	8.5	0.60	0.30	0.15	2.00	1.20
C109	8.5	0.90	0.30	0.15	3.00	1.50
C110	8.5	1.20	0.30	0.15	4.00	1.80
C111	8.5	0.10	0.60	0.15	0.17	1.30
C112	8.5	0.30	0.60	0.15	0.50	1.50
C113	8.5	0.60	0.60	0.15	1.00	1.80
C114	8.5	0.90	0.60	0.15	1.50	2.10
C115	8.5	1.20	0.60	0.15	2.00	2.40
C116	8.5	0.10	0.90	0.15	0.11	1.90
C117	8.5	0.30	0.90	0.15	0.33	2.10
C118	8.5	0.60	0.90	0.15	0.67	2.40
C119	8.5	0.90	0.90	0.15	1.00	2.70
C120	8.5	1.20	0.90	0.15	1.33	3.00
C121	8.5	0.10	1.20	0.15	0.08	2.50
C122	8.5	0.30	1.20	0.15	0.25	2.70
C123	8.5	0.60	1.20	0.15	0.50	3.00
C124	8.5	0.90	1.20	0.15	0.75	3.30
C125	8.5	1.20	1.20	0.15	1.00	3.60
C126	8.5	0.10	0.10	0.10	1.00	0.30
C127	8.5	0.30	0.10	0.10	3.00	0.50
C128	8.5	0.60	0.10	0.10	6.00	0.80
C129	8.5	0.90	0.10	0.10	9.00	1.10
C130	8.5	1.20	0.10	0.10	12.00	1.40
C131	8.5	0.10	0.30	0.10	0.33	0.70

Table A.5: Compositions (C132 - C164) with varying Si, Fe, Mn, Mg (wt%).

Alloy	Si (wt%)	Fe (wt%)	Mn (wt%)	Mg (wt%)	Fe/Mn Ratio	SF
C132	8.5	0.30	0.30	0.10	1.00	0.90
C133	8.5	0.60	0.30	0.10	2.00	1.20
C134	8.5	0.90	0.30	0.10	3.00	1.50
C135	8.5	1.20	0.30	0.10	4.00	1.80
C136	8.5	0.10	0.60	0.10	0.17	1.30
C137	8.5	0.30	0.60	0.10	0.50	1.50
C138	8.5	0.60	0.60	0.10	1.00	1.80
C139	8.5	0.90	0.60	0.10	1.50	2.10
C140	8.5	1.20	0.60	0.10	2.00	2.40
C141	8.5	0.10	0.90	0.10	0.11	1.90
C142	8.5	0.30	0.90	0.10	0.33	2.10
C143	8.5	0.60	0.90	0.10	0.67	2.40
C144	8.5	0.90	0.90	0.10	1.00	2.70
C145	8.5	1.20	0.90	0.10	1.33	3.00
C146	8.5	0.10	1.20	0.10	0.08	2.50
C147	8.5	0.30	1.20	0.10	0.25	2.70
C148	8.5	0.60	1.20	0.10	0.50	3.00
C149	8.5	0.90	1.20	0.10	0.75	3.30
C150	8.5	1.20	1.20	0.10	1.00	3.60
C151	9.0	0.10	0.10	0.20	1.00	0.30
C152	9.0	0.30	0.10	0.20	3.00	0.50
C153	9.0	0.60	0.10	0.20	6.00	0.80
C154	9.0	0.90	0.10	0.20	9.00	1.10
C155	9.0	1.20	0.10	0.20	12.00	1.40
C156	9.0	0.10	0.30	0.20	0.33	0.70
C157	9.0	0.30	0.30	0.20	1.00	0.90
C158	9.0	0.60	0.30	0.20	2.00	1.20
C159	9.0	0.90	0.30	0.20	3.00	1.50
C160	9.0	1.20	0.30	0.20	4.00	1.80
C161	9.0	0.10	0.60	0.20	0.17	1.30
C162	9.0	0.30	0.60	0.20	0.50	1.50
C163	9.0	0.60	0.60	0.20	1.00	1.80
C164	9.0	0.90	0.60	0.20	1.50	2.10

Table A.6: Compositions (C165 - C197) with varying Si, Fe, Mn, Mg (wt%).

Alloy	Si (wt%)	Fe (wt%)	Mn (wt%)	Mg (wt%)	Fe/Mn Ratio	SF
C165	9.0	1.20	0.60	0.20	2.00	2.40
C166	9.0	0.10	0.90	0.20	0.11	1.90
C167	9.0	0.30	0.90	0.20	0.33	2.10
C168	9.0	0.60	0.90	0.20	0.67	2.40
C169	9.0	0.90	0.90	0.20	1.00	2.70
C170	9.0	1.20	0.90	0.20	1.33	3.00
C171	9.0	0.10	1.20	0.20	0.08	2.50
C172	9.0	0.30	1.20	0.20	0.25	2.70
C173	9.0	0.60	1.20	0.20	0.50	3.00
C174	9.0	0.90	1.20	0.20	0.75	3.30
C175	9.0	1.20	1.20	0.20	1.00	3.60
C176	9.0	0.10	0.10	0.15	1.00	0.30
C177	9.0	0.30	0.10	0.15	3.00	0.50
C178	9.0	0.60	0.10	0.15	6.00	0.80
C179	9.0	0.90	0.10	0.15	9.00	1.10
C180	9.0	1.20	0.10	0.15	12.00	1.40
C181	9.0	0.10	0.30	0.15	0.33	0.70
C182	9.0	0.30	0.30	0.15	1.00	0.90
C183	9.0	0.60	0.30	0.15	2.00	1.20
C184	9.0	0.90	0.30	0.15	3.00	1.50
C185	9.0	1.20	0.30	0.15	4.00	1.80
C186	9.0	0.10	0.60	0.15	0.17	1.30
C187	9.0	0.30	0.60	0.15	0.50	1.50
C188	9.0	0.60	0.60	0.15	1.00	1.80
C189	9.0	0.90	0.60	0.15	1.50	2.10
C190	9.0	1.20	0.60	0.15	2.00	2.40
C191	9.0	0.10	0.90	0.15	0.11	1.90
C192	9.0	0.30	0.90	0.15	0.33	2.10
C193	9.0	0.60	0.90	0.15	0.67	2.40
C194	9.0	0.90	0.90	0.15	1.00	2.70
C195	9.0	1.20	0.90	0.15	1.33	3.00
C196	9.0	0.10	1.20	0.15	0.08	2.50
C197	9.0	0.30	1.20	0.15	0.25	2.70

Table A.7: Compositions (C198 - C230) with varying Si, Fe, Mn, Mg (wt%).

Alloy	Si (wt%)	Fe (wt%)	Mn (wt%)	Mg (wt%)	Fe/Mn Ratio	SF
C198	9.0	0.60	1.20	0.15	0.50	3.00
C199	9.0	0.90	1.20	0.15	0.75	3.30
C200	9.0	1.20	1.20	0.15	1.00	3.60
C201	9.0	0.10	0.10	0.10	1.00	0.30
C202	9.0	0.30	0.10	0.10	3.00	0.50
C203	9.0	0.60	0.10	0.10	6.00	0.80
C204	9.0	0.90	0.10	0.10	9.00	1.10
C205	9.0	1.20	0.10	0.10	12.00	1.40
C206	9.0	0.10	0.30	0.10	0.33	0.70
C207	9.0	0.30	0.30	0.10	1.00	0.90
C208	9.0	0.60	0.30	0.10	2.00	1.20
C209	9.0	0.90	0.30	0.10	3.00	1.50
C210	9.0	1.20	0.30	0.10	4.00	1.80
C211	9.0	0.10	0.60	0.10	0.17	1.30
C212	9.0	0.30	0.60	0.10	0.50	1.50
C213	9.0	0.60	0.60	0.10	1.00	1.80
C214	9.0	0.90	0.60	0.10	1.50	2.10
C215	9.0	1.20	0.60	0.10	2.00	2.40
C216	9.0	0.10	0.90	0.10	0.11	1.90
C217	9.0	0.30	0.90	0.10	0.33	2.10
C218	9.0	0.60	0.90	0.10	0.67	2.40
C219	9.0	0.90	0.90	0.10	1.00	2.70
C220	9.0	1.20	0.90	0.10	1.33	3.00
C221	9.0	0.10	1.20	0.10	0.08	2.50
C222	9.0	0.30	1.20	0.10	0.25	2.70
C223	9.0	0.60	1.20	0.10	0.50	3.00
C224	9.0	0.90	1.20	0.10	0.75	3.30
C225	9.0	1.20	1.20	0.10	1.00	3.60
C226	9.5	0.10	0.10	0.20	1.00	0.30
C227	9.5	0.30	0.10	0.20	3.00	0.50
C228	9.5	0.60	0.10	0.20	6.00	0.80
C229	9.5	0.90	0.10	0.20	9.00	1.10
C230	9.5	1.20	0.10	0.20	12.00	1.40

Table A.8: Compositions (C231 - C263) with varying Si, Fe, Mn, Mg (wt%).

Alloy	Si (wt%)	Fe (wt%)	Mn (wt%)	Mg (wt%)	Fe/Mn Ratio	SF
C231	9.5	0.10	0.30	0.20	0.33	0.70
C232	9.5	0.30	0.30	0.20	1.00	0.90
C233	9.5	0.60	0.30	0.20	2.00	1.20
C234	9.5	0.90	0.30	0.20	3.00	1.50
C235	9.5	1.20	0.30	0.20	4.00	1.80
C236	9.5	0.10	0.60	0.20	0.17	1.30
C237	9.5	0.30	0.60	0.20	0.50	1.50
C238	9.5	0.60	0.60	0.20	1.00	1.80
C239	9.5	0.90	0.60	0.20	1.50	2.10
C240	9.5	1.20	0.60	0.20	2.00	2.40
C241	9.5	0.10	0.90	0.20	0.11	1.90
C242	9.5	0.30	0.90	0.20	0.33	2.10
C243	9.5	0.60	0.90	0.20	0.67	2.40
C244	9.5	0.90	0.90	0.20	1.00	2.70
C245	9.5	1.20	0.90	0.20	1.33	3.00
C246	9.5	0.10	1.20	0.20	0.08	2.50
C247	9.5	0.30	1.20	0.20	0.25	2.70
C248	9.5	0.60	1.20	0.20	0.50	3.00
C249	9.5	0.90	1.20	0.20	0.75	3.30
C250	9.5	1.20	1.20	0.20	1.00	3.60
C251	9.5	0.10	0.10	0.15	1.00	0.30
C252	9.5	0.30	0.10	0.15	3.00	0.50
C253	9.5	0.60	0.10	0.15	6.00	0.80
C254	9.5	0.90	0.10	0.15	9.00	1.10
C255	9.5	1.20	0.10	0.15	12.00	1.40
C256	9.5	0.10	0.30	0.15	0.33	0.70
C257	9.5	0.30	0.30	0.15	1.00	0.90
C258	9.5	0.60	0.30	0.15	2.00	1.20
C259	9.5	0.90	0.30	0.15	3.00	1.50
C260	9.5	1.20	0.30	0.15	4.00	1.80
C261	9.5	0.10	0.60	0.15	0.17	1.30
C262	9.5	0.30	0.60	0.15	0.50	1.50
C263	9.5	0.60	0.60	0.15	1.00	1.80

Table A.9: Compositions (C264 - C300) with varying Si, Fe, Mn, Mg (wt%).

Alloy	Si (wt%)	Fe (wt%)	Mn (wt%)	Mg (wt%)	Fe/Mn Ratio	SF
C264	9.5	0.90	0.60	0.15	1.50	2.10
C265	9.5	1.20	0.60	0.15	2.00	2.40
C266	9.5	0.10	0.90	0.15	0.11	1.90
C267	9.5	0.30	0.90	0.15	0.33	2.10
C268	9.5	0.60	0.90	0.15	0.67	2.40
C269	9.5	0.90	0.90	0.15	1.00	2.70
C270	9.5	1.20	0.90	0.15	1.33	3.00
C271	9.5	0.10	1.20	0.15	0.08	2.50
C272	9.5	0.30	1.20	0.15	0.25	2.70
C273	9.5	0.60	1.20	0.15	0.50	3.00
C274	9.5	0.90	1.20	0.15	0.75	3.30
C275	9.5	1.20	1.20	0.15	1.00	3.60
C276	9.5	0.10	0.10	0.10	1.00	0.30
C277	9.5	0.30	0.10	0.10	3.00	0.50
C278	9.5	0.60	0.10	0.10	6.00	0.80
C279	9.5	0.90	0.10	0.10	9.00	1.10
C280	9.5	1.20	0.10	0.10	12.00	1.40
C281	9.5	0.10	0.30	0.10	0.33	0.70
C282	9.5	0.30	0.30	0.10	1.00	0.90
C283	9.5	0.60	0.30	0.10	2.00	1.20
C284	9.5	0.90	0.30	0.10	3.00	1.50
C285	9.5	1.20	0.30	0.10	4.00	1.80
C286	9.5	0.10	0.60	0.10	0.17	1.30
C287	9.5	0.30	0.60	0.10	0.50	1.50
C288	9.5	0.60	0.60	0.10	1.00	1.80
C289	9.5	0.90	0.60	0.10	1.50	2.10
C290	9.5	1.20	0.60	0.10	2.00	2.40
C291	9.5	0.10	0.90	0.10	0.11	1.90
C292	9.5	0.30	0.90	0.10	0.33	2.10
C293	9.5	0.60	0.90	0.10	0.67	2.40
C294	9.5	0.90	0.90	0.10	1.00	2.70
C295	9.5	1.20	0.90	0.10	1.33	3.00
C296	9.5	0.10	1.20	0.10	0.08	2.50
C297	9.5	0.30	1.20	0.10	0.25	2.70
C298	9.5	0.60	1.20	0.10	0.50	3.00
C299	9.5	0.90	1.20	0.10	0.75	3.30
C300	9.5	1.20	1.20	0.10	1.00	3.60

Table A.10: Compositions (C301 - C312) with varying Si, Fe, Mn, Mg (wt%).

Alloy	Si (wt%)	Fe (wt%)	Mn (wt%)	Mg (wt%)	Fe/Mn Ratio	SF
C301	8.5	0.60	0.30	0.50	2.00	1.20
C302	8.5	0.60	0.30	1.00	2.00	1.20
C303	8.5	0.10	0.50	0.20	0.20	1.10
C304	8.5	0.20	1.00	0.20	0.20	2.20
C305	8.5	0.30	0.10	0.20	3.00	0.50
C306	8.5	0.60	0.20	0.20	3.00	1.00
C307	8.5	1.20	0.40	0.20	3.00	2.00
C308	9.5	0.10	0.50	0.16	0.20	1.10
C309	9.5	0.20	1.00	0.16	0.20	2.20
C310	9.5	0.30	0.10	0.16	3.00	0.50
C311	9.5	0.60	0.20	0.16	3.00	1.00
C312	9.5	1.20	0.40	0.16	3.00	2.00

B

SEM-, EDS-, point- and map images

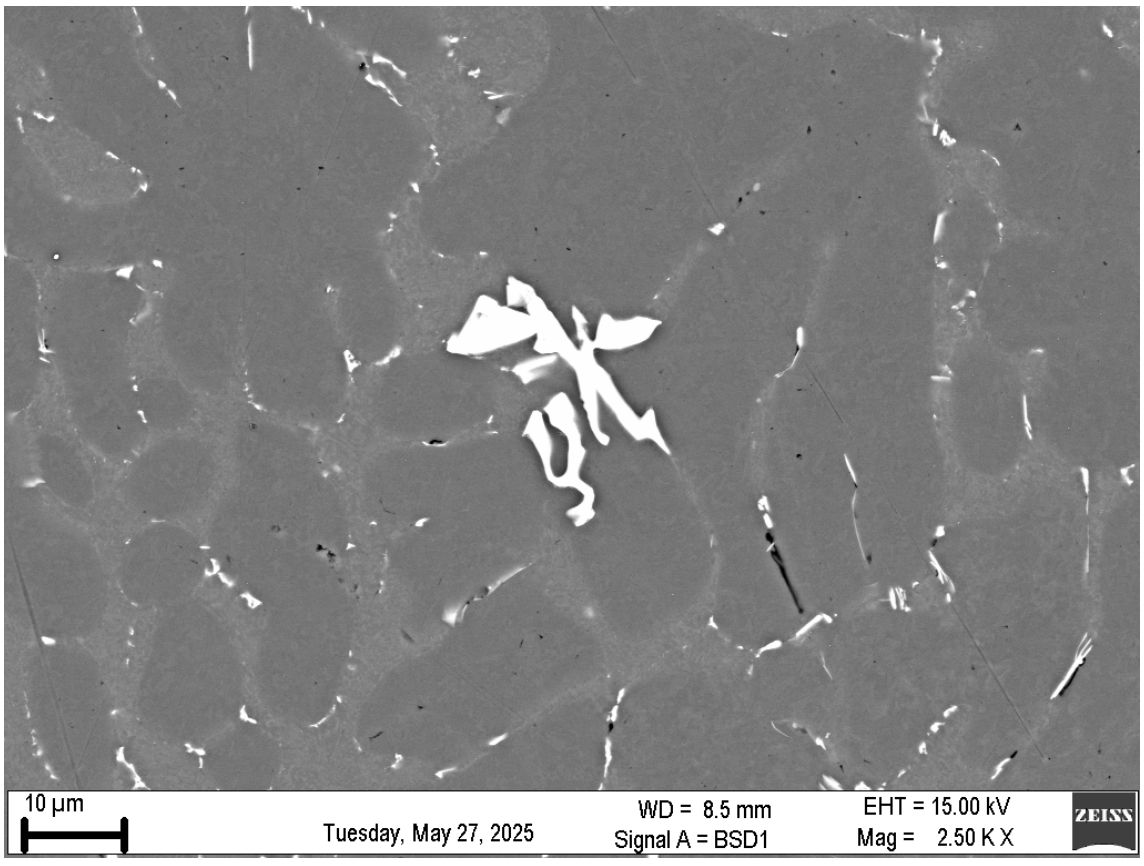

Figure B.1: SEM image showing full view of alpha phase Chinese scrip like intermetallic in A1.

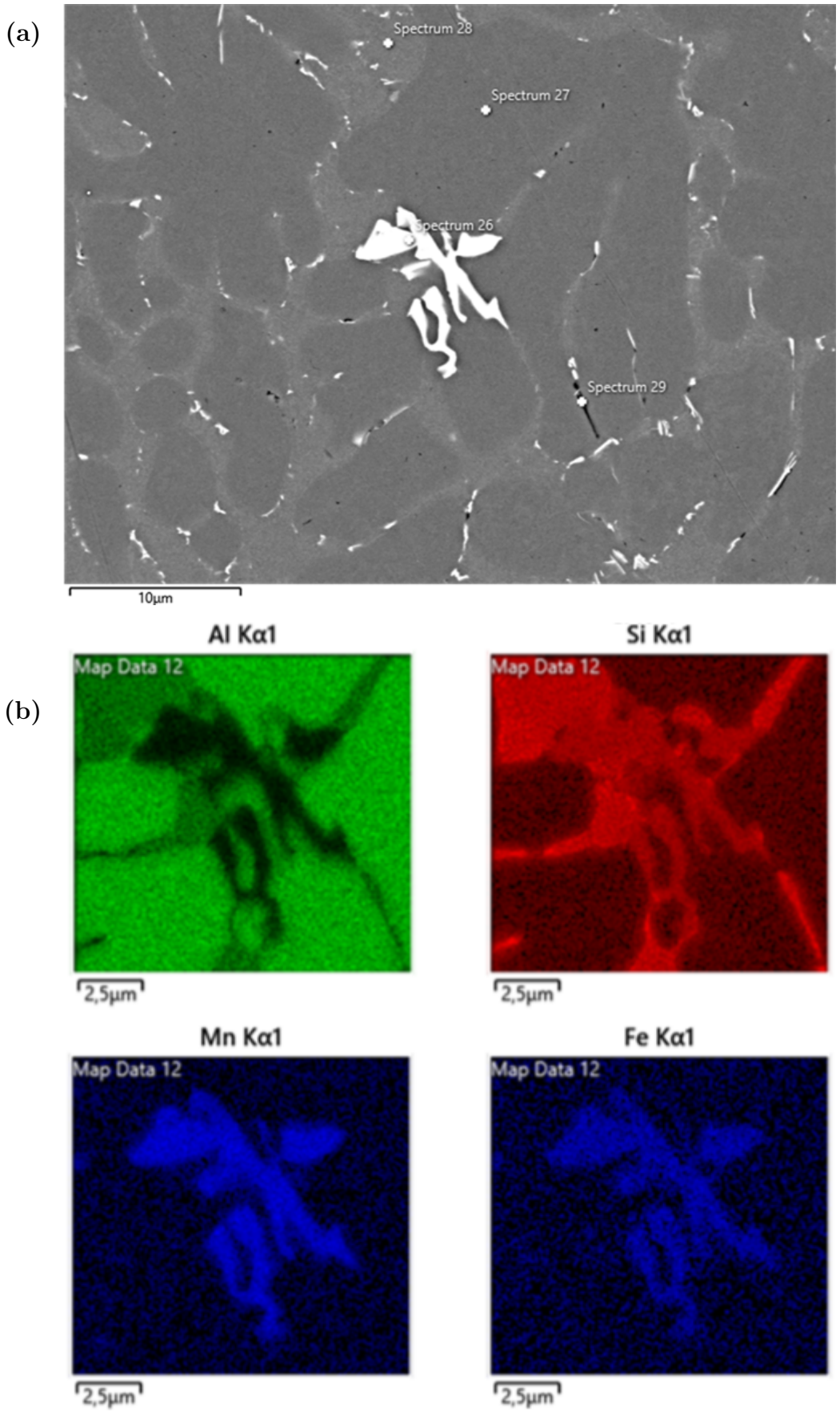

Figure B.2: Sample A1 showing α-phase: (a) Point map, (b) EDS-mapping

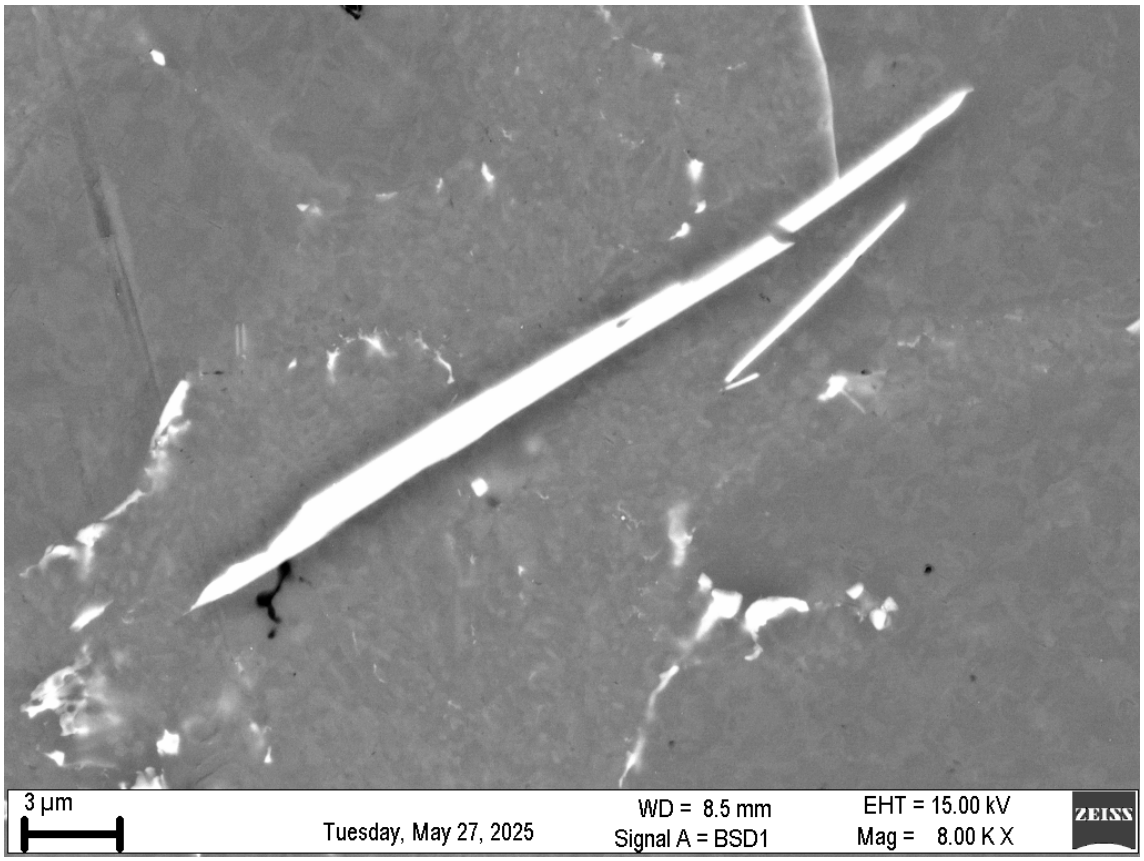

Figure B.3: SEM image showing the Morphology of a typical needle like beta phase in A1.

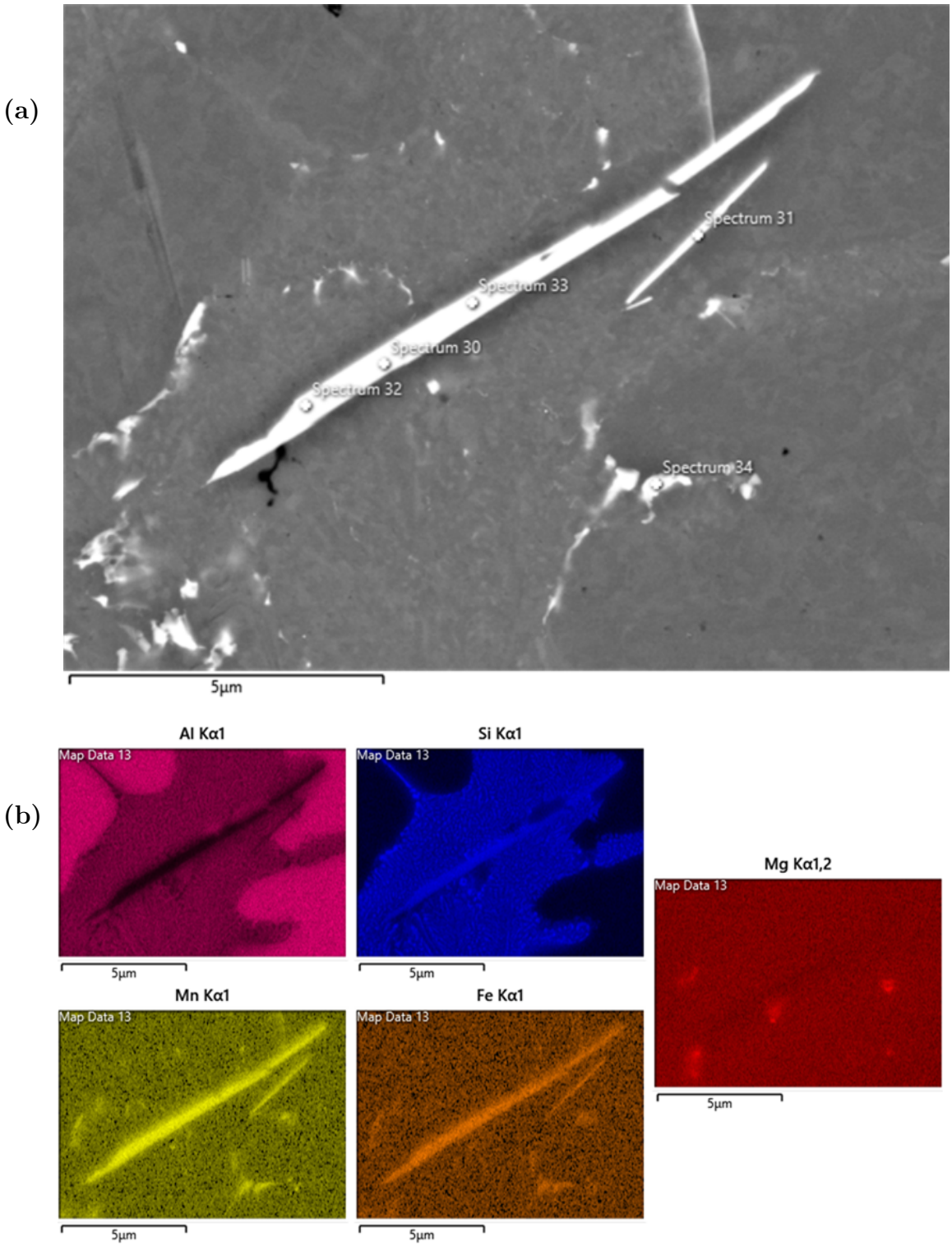

Figure B.4: Sample A1 showing β-phase: (a) Point map, (b) EDS-mapping

(a)

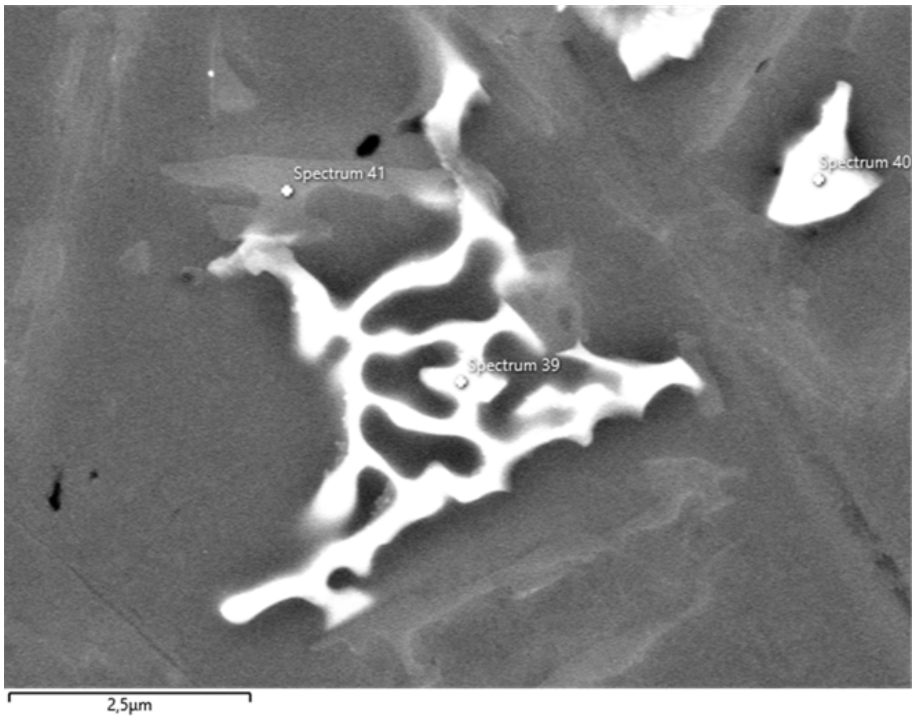

(b)

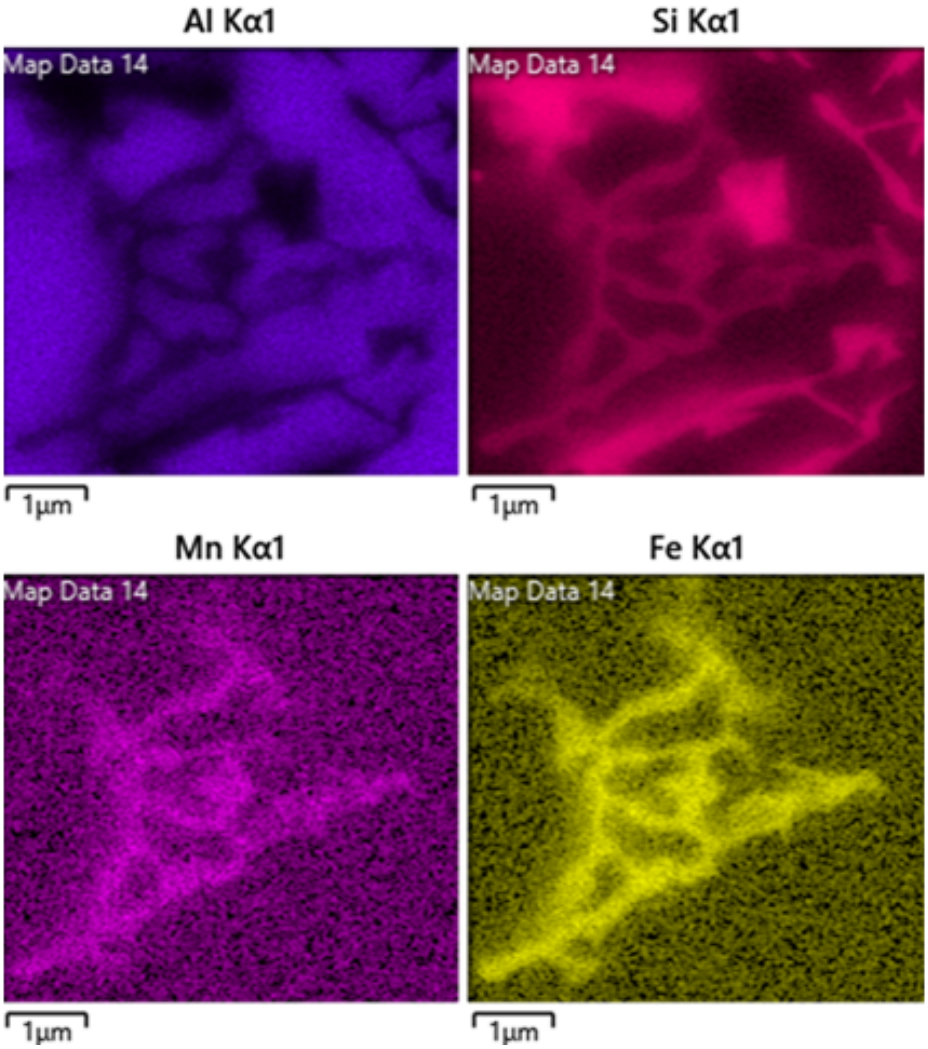

Figure B.5: Sample A4 showing α-phase: (a) Point map, (b) EDS-mapping

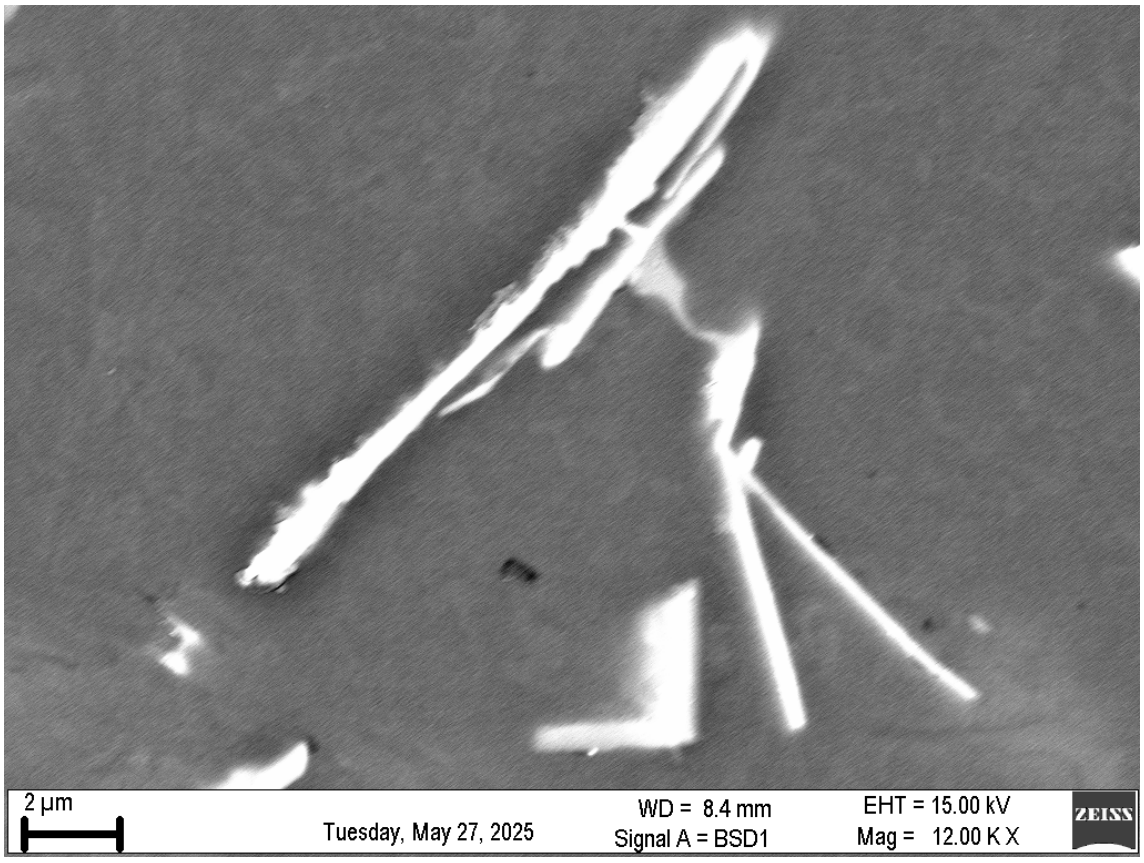

Figure B.6: SEM image showing the Morphology of a typical needle like beta phase in A4.

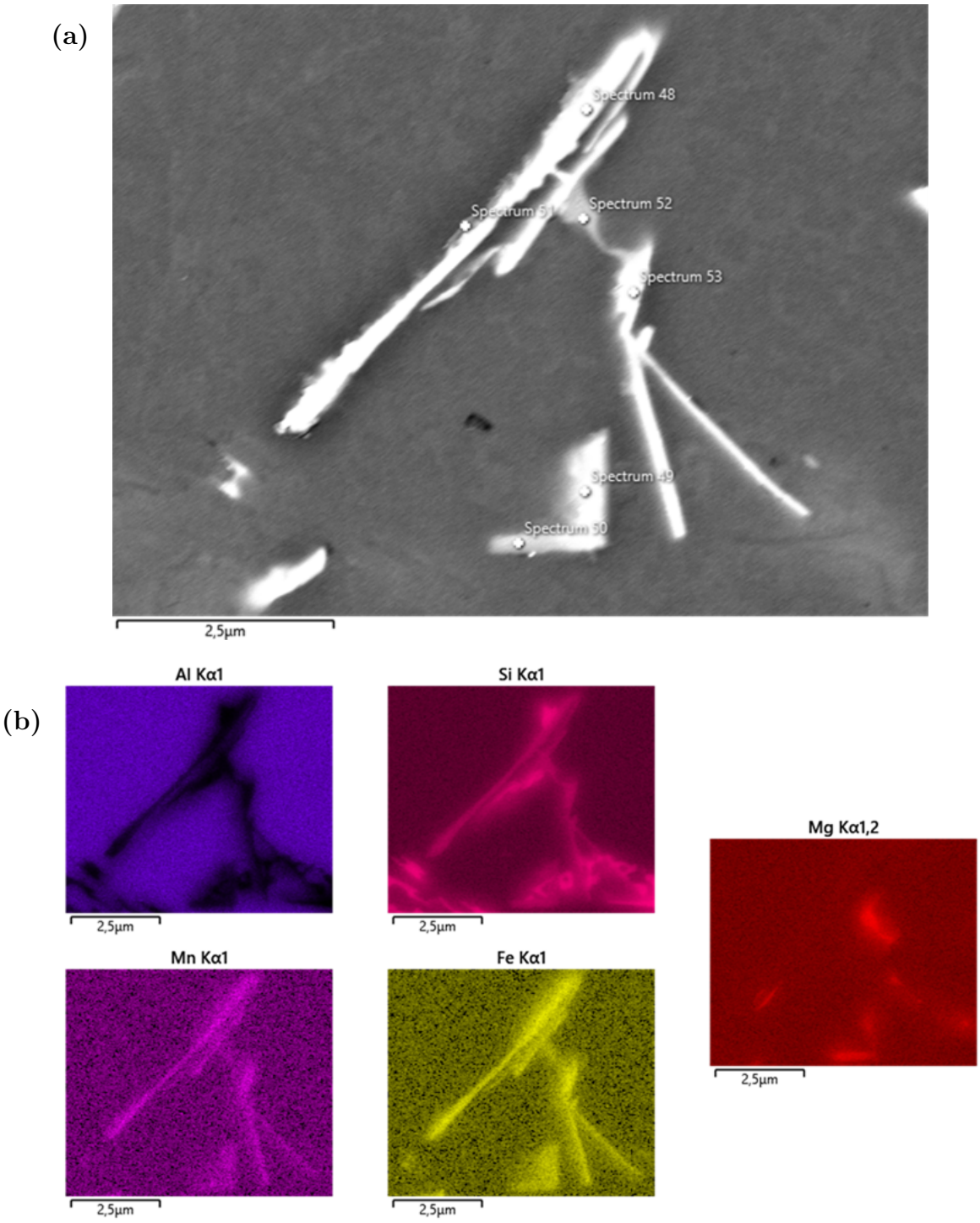

Figure B.7: Sample A4 showing β-phase: (a) Point map, (b) EDS-mapping

DEPARTMENT OF SOME SUBJECT OR TECHNOLOGY
CHALMERS UNIVERSITY OF TECHNOLOGY
Gothenburg, Sweden
www.chalmers.se

CHALMERS
UNIVERSITY OF TECHNOLOGY